Pacific Northwest
NATIONAL LABORATORY

PNNL-34984 Rev 0
DVZ-RPT-099 Rev 0

Using Geophysical Information to Investigate Subsurface Structure within the High-Hydraulic Conductivity Analysis Zone

September 2023

Judy Robinson
James St. Clair
Jon Thomle
Joaquin Cambeiro
Jonah Bartrand

U.S. DEPARTMENT OF ENERGY

Prepared for the U.S. Department of Energy
under Contract DE-AC05-76RL01830

PACIFIC NORTHWEST NATIONAL LABORATORY
operated by
BATTELLE
for the
UNITED STATES DEPARTMENT OF ENERGY
under Contract DE-AC05-76RL01830

Printed in the United States of America

Available to DOE and DOE contractors from the
Office of Scientific and Technical Information,
P.O. Box 62, Oak Ridge, TN 37831-0062;
ph: (865) 576-8401
fax: (865) 576-5728
email: reports@adonis.osti.gov

Available to the public from the National Technical Information Service
5301 Shawnee Rd., Alexandria, VA 22312
ph: (800) 553-NTIS (6847)
email: orders@ntis.gov <https://www.ntis.gov/about>
Online ordering: http://www.ntis.gov

PNNL-34984 Rev 0
DVZ-RPT-099 Rev 0

Using Geophysical Information to Investigate Subsurface Structure within the High-Hydraulic Conductivity Analysis Zone

September 2023

Judy Robinson
James St. Clair
Jon Thomle
Joaquin Cambeiro
Jonah Bartrand

Prepared for
the U.S. Department of Energy
under Contract DE-AC05-76RL01830

Pacific Northwest National Laboratory
Richland, Washington 99354

Summary

Within the 200 East Area of the Central Plateau and southeastward toward the Columbia River, a high-hydraulic conductivity zone (HCZ) has been interpreted to extend through the 200-PO-1 and 200-BP-5 operable units on the Hanford Site. The HCZ is a controlling hydraulic feature that impacts groundwater flow out of the 200 East Area and the fate of eastwardly migrating plumes from the 200 West Area. The lateral extent of the HCZ is highly uncertain, and despite strong evidence for the existence of the HCZ based on water-level data and contaminant plume tracking, there is still a limited understanding of how to define its boundaries. To provide additional information on the nature and extent of the HCZ, three surface geophysical methods – electrical resistivity tomography (ERT), time-domain electromagnetics (TEM), and seismic methods – were used to collect data south of 200 East. In addition, existing data from 200 East, consisting of surface seismic data, a borehole check shot survey in 699-37-47A, and borehole stratigraphic interpretations, were used to aid interpretations of newly collected seismic data south of 200 East. This work presumed that the contrast in subsurface geophysical properties would be a first-order aid identifying a transmissive zone(s) within the HCZ analysis area by imaging contrasts and/or anomalies in geophysical properties. While seismic, ERT, and TEM methods have sensitivity to overlapping physical properties (porosity, moisture content, lithology), the resolution and physics used to acquire each of these datasets are different, and therefore the information can also be different. Figure S.1 shows the locations of the geophysical data considered in this report.

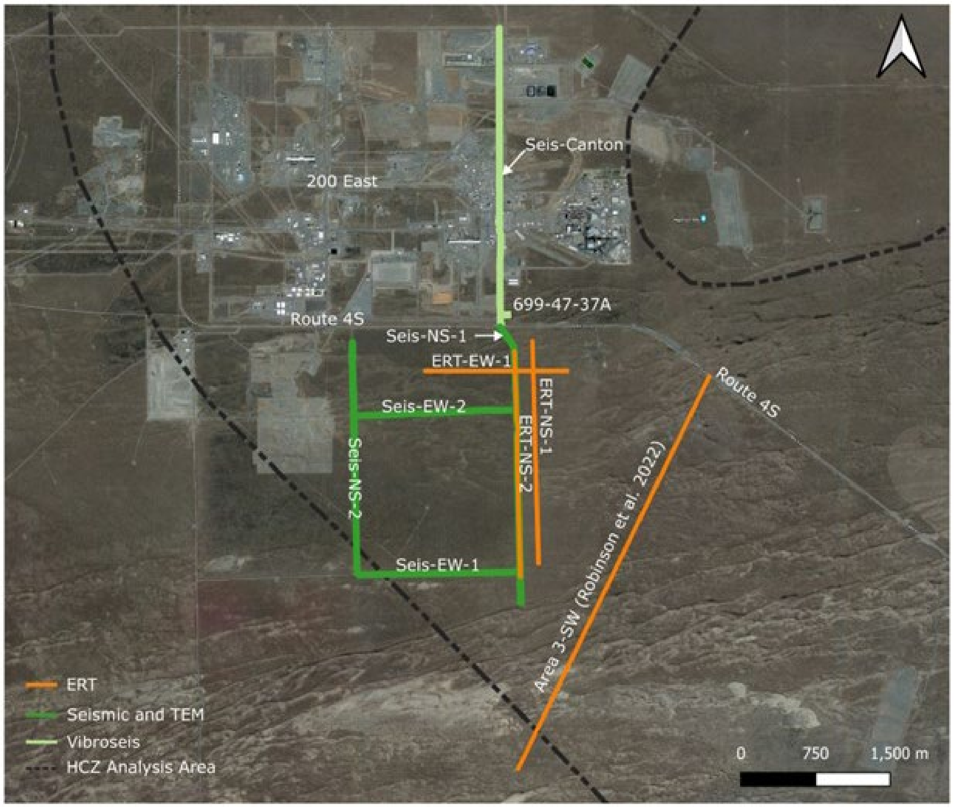

Figure S.1. Geophysical profiles for ERT (NS-1, NS-2, EW-1), seismic (NS-1, NS-2, EW-1, EW-2), and vibroseis seismic (Canton) within and south of 200 East within the HCZ analysis area. A previously acquired ERT profile (Area 3-SW[1]) is also shown.

The interpretation of the combined ERT/seismic/TEM dataset is performed in the context of a conceptual model for the HCZ analysis area in which the transmissive pathways within the HCZ are hypothesized to be coarse-grained and more permeable material incised into less permeable units. Commonly, coarser grained materials exhibit higher bulk electrical conductivity (EC), thus providing a signature with respect to ERT and tTEM. Coarse-grained, unconsolidated materials commonly exhibit lower seismic velocity compared to more cemented and stiffer finer-grained materials, thus providing a signature with respect to seismic methods. Additionally, seismic reflections can occur from interfaces with subtle variations in seismic properties, enabling identification of stratigraphic contacts or incised channels. The conceptual model provides a framework to develop an integrated interpretation of the three geophysical datasets. Such combined interpretation tends to reduce uncertainty compared to interpretation of a single dataset by addressing issues of non-uniqueness associated with the sensitivity of a single geophysical method to multiple factors.

The ERT results show similarities and variations in subsurface structure between transects and overall consistency with the seismic results. The eastern section of an east-west (EW) ERT profile has a similar profile image compared to Area 3-SW, which is further to the south and east. Both ERT profiles show a low bulk EC layer, presumed in previous studies to be less consolidated sandy-gravel deposits, overlying a more conductive layer, presumed in previous studies to be more consolidated and/or finer deposits. This contrasts with north-south (NS) ERT profiles, which show a higher relative bulk EC and limited structure

[1] Robinson, J., J. Thomle, D. McFarland, K. Deters, M. Rockhold, F. Day-Lewis and V. Freedman (2022). "Integration of Large-Scale Electrical Imaging into Geological Framework Development and Refinement." Environmental Processes 9(2).

at shallower depths compared to other profiles (Figure S.2). The difference between the eastern EW and NS ERT profiles may indicate a contrast in porosity and/or moisture content; however, the contrast is small and did not manifest a seismic signature. Given the lack of seismic signature and relatively small contrast in bulk EC, the feature observed on NS-1 and NS-2 is not interpreted as being within the HCZ analysis area but instead is attributed to variations in moisture of fluid conductivity compared to the other lines. However, future work could assess this interpretation using direct measurements of permeability. Coincident NS ERT and seismic images show shallow structural similarity; however, they have limited similarity at depths > 50 m, where the higher bulk EC region is present.

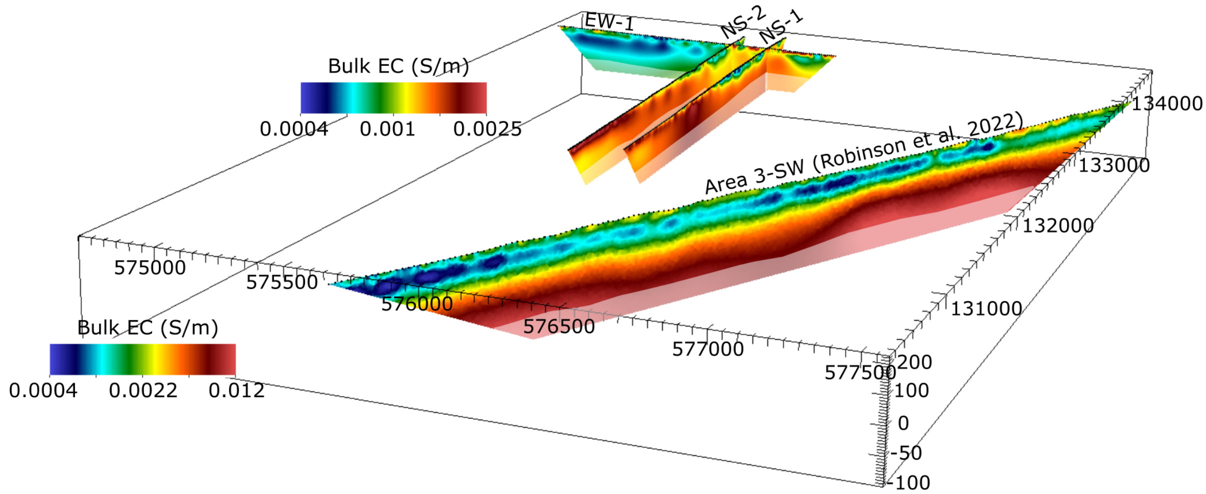

Figure S.2. ERT summary south of 200 East showing difference in bulk EC structure along NS-1 and NS-2 compared to other images.

The shallow seismic images (> 0 m elevation; 175-200 m bgs) provide information on stratigraphic unit orientation and the presence of units and show a horizontal north-dipping layered structure (Figure S.3). Independent processing of seismic reflection and compressional wave velocities (Vp) from seismic tomography agreed well, and interpretations were guided by available borehole stratigraphic interpretations and a check shot survey in a nearby borehole (699-37-47A). These images (Figure S.3) reveal that higher Vp basalt (dark blue in the figure) becomes deeper moving south (Seis-Canton); newly collected profiles (Seis-NS-1, Seis-NS-2, Seis-EW-1, Seis-EW-2) did not detect the higher Vp indicative of basalt. Figure S.3 also shows that the Vp layer representative of Ringold sediments (yellow to light blue) is thicker moving south along the seismic profiles. The seismic reflection data also contained information on a deeper reflector, which may be imaging interbedding within the basalt. In previous stratigraphic identification tasks at Hanford, this has not been previously identified using geophysical datasets. The seismic results provide information to confirm and refine the hydrogeologic framework of the area but provide no clear indication of paleochannels associated with the HCZ analysis area in the form of velocity contrasts or reflections.

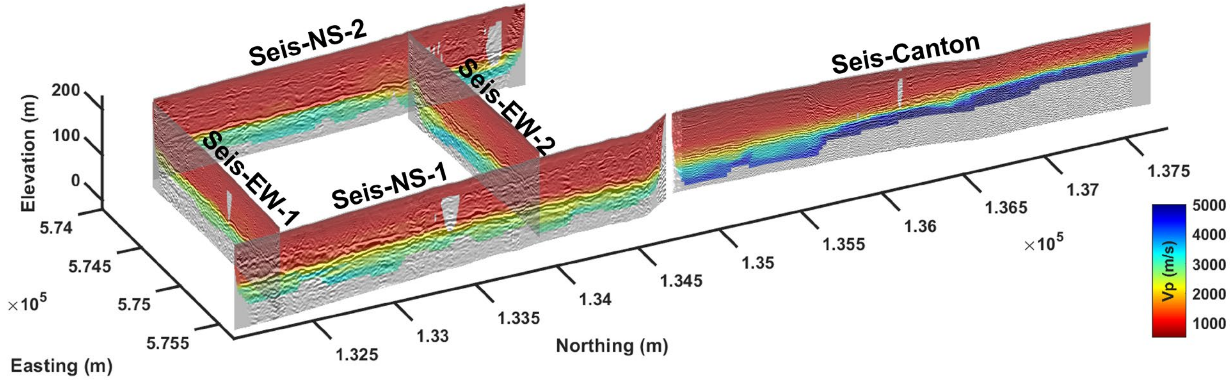

Figure S.3. Compressional wave velocities (Vp, color scale) and seismic reflection (gray scale) images shown as a fence diagram.

TEM data proved to be unusable due to interfering anthropogenic coupling (e.g., power lines) and the presence of a thick, overlying low-conductivity Hanford unit that limited signal magnitudes. It is recommended that this method be used at Hanford where the water table and/or low-conductivity units are shallower.

Using geophysical methods within and south of 200 East provided qualitative information on stratigraphic structure. ERT images were qualitatively compared to each other and to other images previously collected. Supporting borehole data allowed for more than qualitative seismic interpretations, and stratigraphic units could be interpreted. Additional site testing (e.g., hydraulic testing) and data (borehole ERT, seismic, borehole stratigraphic interpretations) will support and add to the interpretations in this report. Newer machine-learning methods might also be used to calibrate a site-specific Hanford model, adding insight to these interpretations to use in flow and transport simulations to better understand contaminant migration on the Hanford Central Plateau for remedial planning and decisions.

Acknowledgments

This document was prepared by the Deep Vadose Zone – Applied Field Research Initiative at Pacific Northwest National Laboratory. Funding was provided by the U.S. Department of Energy (DOE) Richland Operations Office. Pacific Northwest National Laboratory is operated by Battelle Memorial Institute for the DOE under Contract DE-AC05-76RL01830.

Acronyms and Abbreviations

AWD	accelerated weight drop
Ba	Columbia River Basalt group
CCU	Cold Creek unit
CMP	Common Midpoint
E4D	geophysical modeling and inversion code used for ERT data inversion
EC	electrical conductivity
EM	electromagnetics
ERT	electrical resistivity tomography
E-W	east-west
GFM	geologic framework model
HCZ	hydraulic conductivity zone
Hf	Hanford formation
MASW	multi-channel analysis of surface waves
N-S	north-south
NE	northeast
NMO	normal moveout
P	parallel
P2R	Plateau to River
PSDM	pre-stack depth migration
Rlm	lower mud unit
Rtf	member of Taylor Flat
RTM	Radio Trigger Module
Rwia	member of Wooded Island, Unit A
Rwie	member of Wooded Island, Unit E
SW	southwest
TEM	time-domain electromagnetics
tTEM	towed time-domain electromagnetics
tt2w	two-way travel time
WDC	Weight Drop Controller

Contents

Figures

Tables

1.0 Introduction

There is a need to identify preferential flow paths and stratigraphic features on the Hanford Site Central Plateau that influence groundwater flow and contaminant transport. These features promote fast groundwater flow because they contain a large amount of gravel and less silt and sand relative to other portions of the aquifer (Martin 2010). These locations extend over kilometers and have been inferred from existing well information, such as groundwater levels and contaminant plume distribution, borehole logs, and hydraulic testing.

One such high-transmissivity location has been designated as the high-hydraulic conductivity aquifer zone (HCZ), which extends through the 200-PO-1 and 200-BP-5 operable units within the 200 East Area of the Central Plateau and southeastward toward the Columbia River. The HCZ is interpreted to be a controlling hydraulic feature that impacts groundwater flow out of the 200 East Area and the fate of eastwardly migrating plumes from the 200 West Area. The most recent HCZ conceptual model analysis area has been drawn from hydraulic head monitoring in the 200 East Area, saturated zone modeling contained in the Plateau to River (P2R) model (Budge 2020), a hydraulic conductivity estimate from well drawdown pump tests in the B Complex (McDonald 2016), and delineation of a low hydraulic gradient zone (CPCCo 2021). While the HCZ analysis area was hypothesized from this information, it is highly uncertain in terms of lateral extent. Surface geophysics including electrical resistivity tomography (ERT), time-domain electromagnetics (TEM), and seismic methods, are being used as minimally invasive and cost-effective tools to investigate and provide information to better define the HCZ. This information could then be used in flow and transport simulations to better understand contaminant migration on the Hanford Central Plateau for remedial planning and decisions.

Geophysical methods have been widely used for detection and delineation of diverse near-surface structures by exploiting the contrasts in subsurface physical properties such as bulk electrical conductivity and seismic wave velocities. Previously, geophysical investigations (ERT, TEM, and seismic) were undertaken within areas of the Central Plateau where high transmissive zones were suspected but there was a limited number of boreholes to delineate with high certainty (Robinson et al. 2020, Robinson et al. 2022, Robinson et al. 2023). ERT images were used as a first line of evidence of subsurface structure and compared to the geological framework model (GFM). Where available, the ERT images were also compared to borehole stratigraphic interpretations, and there was general agreement with location of the electrical contrasts. A quasi-3D inversion was performed between the 200 Areas and a dipping low bulk electrical conductivity (EC) region was identified as a potential area of a high transmissive zone. Seismic data was collected along two ERT profiles, and refraction tomography and reflection images showed general agreement with the ERT images between the 200 Areas, giving confidence to the quasi-3D inversion of ERT data. TEM data had limited success and was found to work well southeast of the 200 East Area where the Hanford formation was not as thick.

Identifying the HCZ based on lithology and/or stratigraphy from boreholes has proven to be challenging, and the current understanding is that hydraulic testing is the best method to delineate the HCZ (CPCCo 2021). This is due to the variability in hydrostratigraphic units, which can translate to lithologic characterizations not reliably yielding information about aquifer hydraulic conductivity, which is the primary identifier of the HCZ. Geophysical methods are sensitive to multiple subsurface properties, for example, porosity, moisture content, and lithology (Archie 1942, Wyllie et al. 1956, Mavko et al. 2009). Previous studies have independently and jointly analyzed electrical and seismic methods for a comprehensive interpretation. For example, Thayer et al. (2018) determined hydrologic portioning of snowmelt by using ERT to monitor moisture content and seismic refraction tomography to identify regolith structure. Carollo et al. (2020) independently inverted seismic refraction and ERT data and then used k-means cluster analysis to jointly interpret the subsurface. Previous work on the Hanford Site

(Robinson et al. 2023) compared ERT and seismic refraction tomography images. These studies show that using multiple geophysical technologies could potentially provide independent or joint information on the existence of the HCZ.

In this work, surface ERT, TEM, and seismic methods were used to investigate an area within the HCZ analysis area on the Central Plateau. Transmissive pathways within the HCZ analysis area are hypothesized to be coarse material incised into less-permeable units, so geophysical investigations were undertaken to identify where contrasts in geophysical properties could be a proxy for subsurface changes in material properties. In addition to newly collected data, previously collected seismic data in the 200 East Area was reprocessed and compared to borehole logs and a seismic check shot previously collected in 699-37-47A. This work presumed that the contrast in subsurface geophysical properties would be a first-order aid identifying a transmissive zone(s) within the HCZ analysis area by imaging contrasts and/or anomalies in geophysical properties. This report details these field and reprocessing investigations and provides a comparative and interpretative analysis.

2.0 Site Description and Geophysical Surveys

The focus area for this study was within and south of the 200 East Area on the Central Plateau, which is within the bounds of the P2R model (Budge 2020). Within the P2R model, the delineation of an HCZ analysis area was hypothesized to represent the location where ancestral flood events formed gravel deposits that are highly permeable and influence the rate and direction of groundwater flow (Budge 2020). An aerial view of nitrate, iodine-129, and tritium plumes (https://phoenix.pnnl.gov) demonstrates a northwest to southeast migration (Figure 1), which exemplifies the orientation and location of the HCZ analysis area.

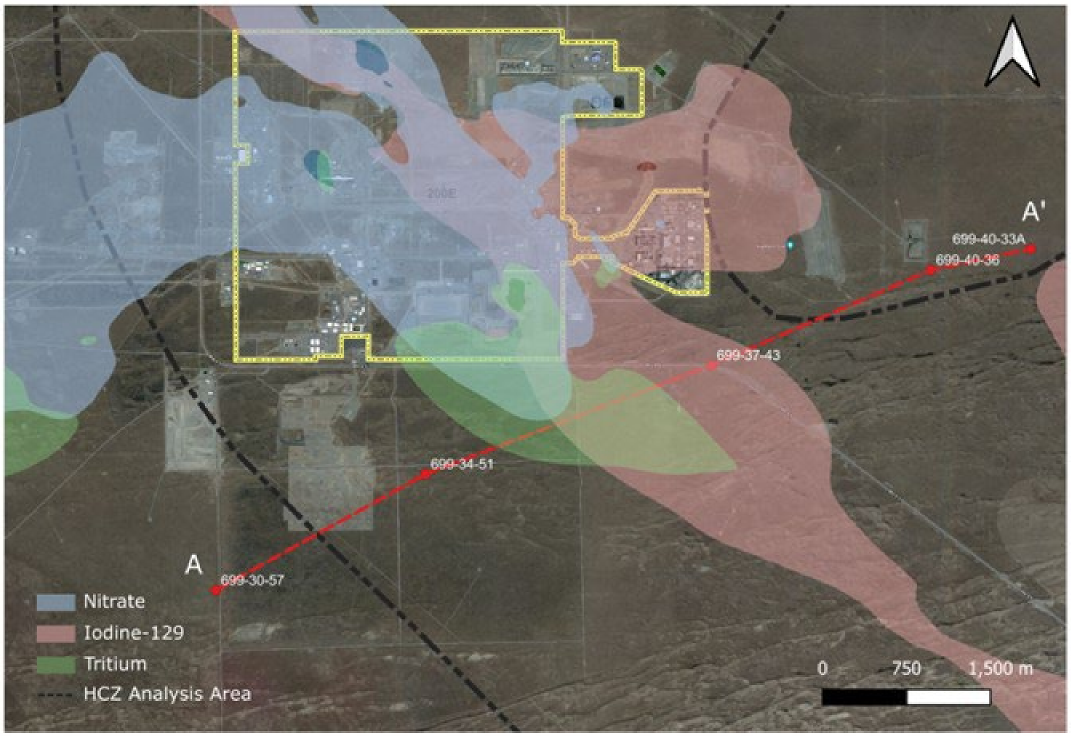

Figure 1. Site map with plume overlay (https://phoenix.pnnl.gov/phoenix/apps/gisexplorer/index.html).

Figure 2 shows an interpolated stratigraphic cross section; the potential lateral extent of the HCZ is denoted. The stratigraphic sequence shown in this cross section consists of four major hydrostratigraphic units: the Hanford formation (Hf), the Cold Creek unit (CCU), the Ringold Formation, and the Columbia River Basalt group (Ba). The Hf consists of glacio-fluvial deposits associated with cataclysmic Ice Age flooding; the CCU contains alluvial, fluvial, and paleosol deposits; and the Ringold Formation consists of alluvial and lacustrine deposits. These units are further subdivided based on proximity to ancient river systems and floodpaths into member of Taylor Flat (Rtf); member of Wooded Island, Unit E (Rwie); the lower mud unit (Rlm); and member of Wooded Island, Unit A (Rwia). In this area, the HCZ is hypothesized to be represented by the CCU and Rtf, and confined by the Rlm. Readers are encouraged to review Martin (2010) and DOE (2002) for more details.

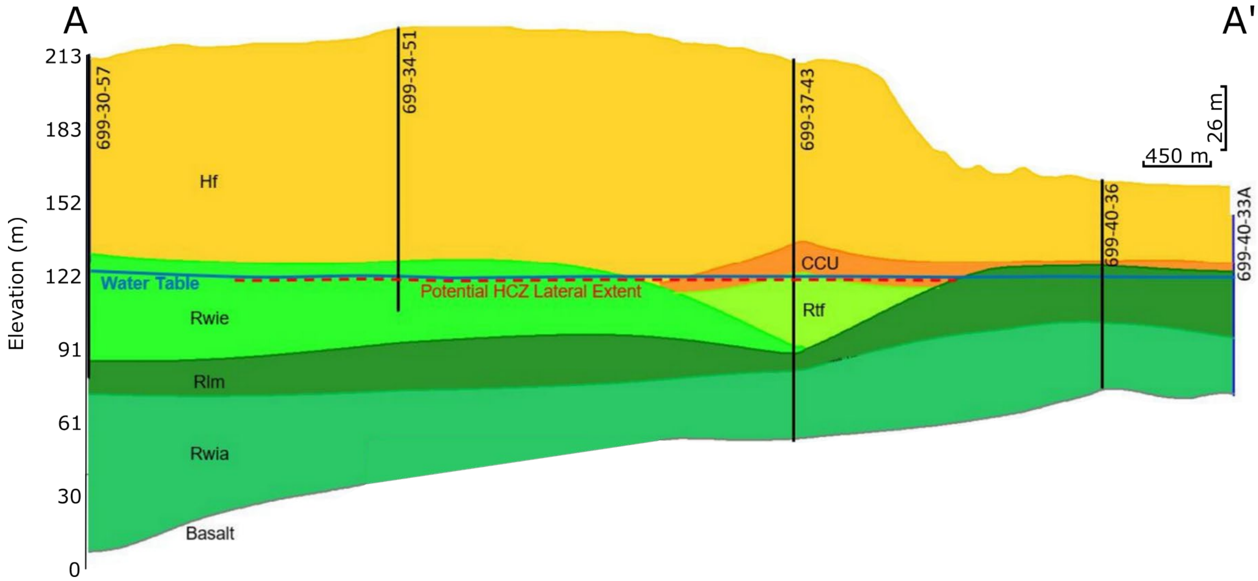

Figure 2. Cross section A-A’ (refer to Figure 1) from the Hanford Site South Geoframework Model (CPCCo 2021, Fig 4)

ERT, TEM, and seismic data were collected south of the 200 East Area (Figure 3). Seismic and TEM data were collected along existing roadways to avoid biological and cultural disturbances of the natural habitat. ERT data was collected along two profiles located off-road and parallel to existing roads; one profile was collected along a roadway to have co-located data from the three geophysical methods. In addition, seismic reflection data from 2008 collected in the 200 East Area along Canton Ave was reprocessed. This data (Figure 3, Seis-Canton) was originally acquired to assess the utility of seismic reflection to improve the geologic conceptual model (CH2M 2009).

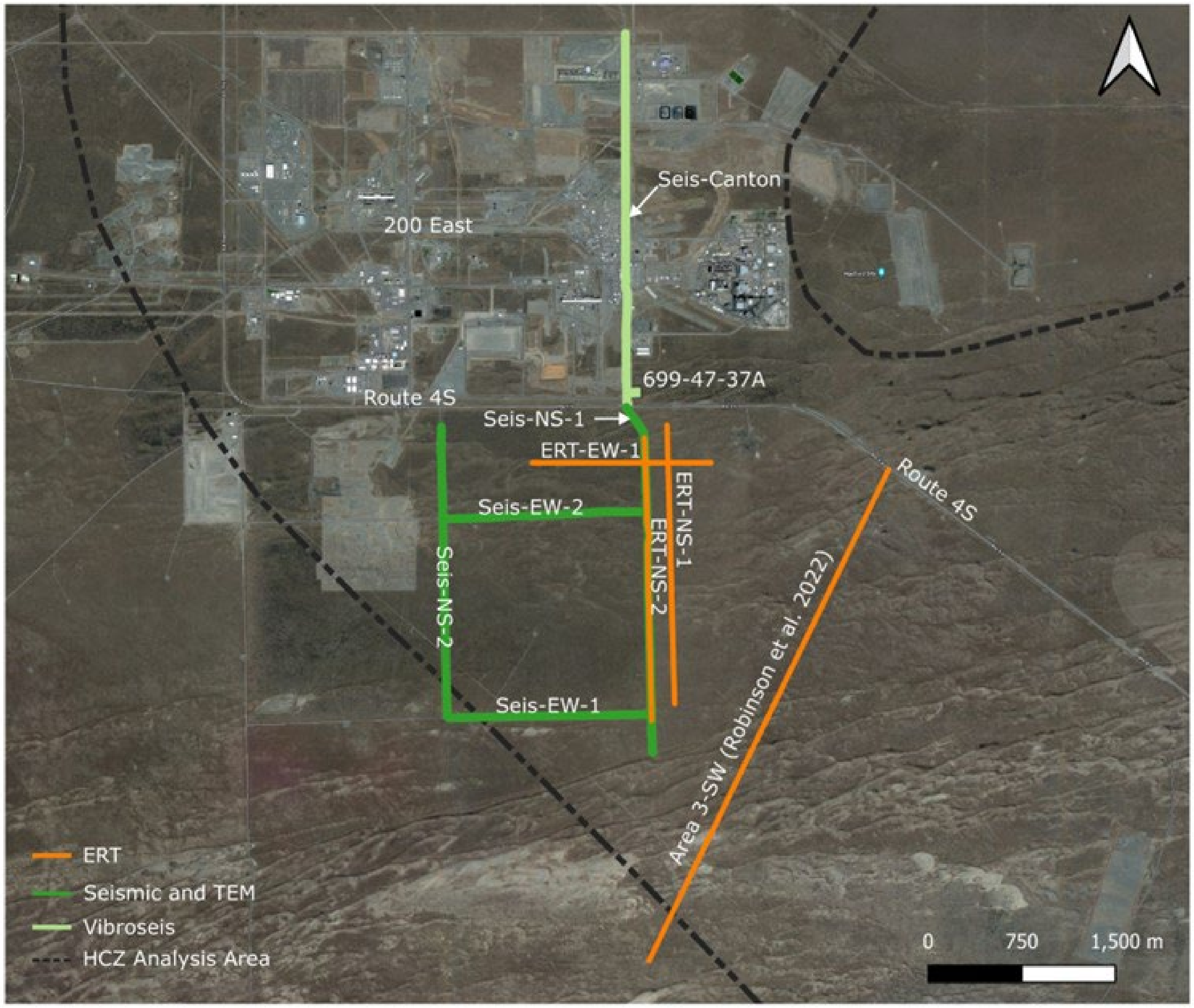

Figure 3. Geophysical profiles for ERT (NS-1, NS-2, EW-1), seismic (NS-1, NS-2, EW-1, EW-2), and vibroseis seismic (Canton) within and south of 200 East within the HCZ analysis area. Also shown are the location of the borehole where seismic check shot data was available (699-47-37A) and Area 3-SW (Robinson et al. 2022).

3.0 Geophysical Methods

This section provides an overview of the ERT, TEM, and seismic refraction tomography methods. See Robinson et al. (2023) for additional information.

3.1 Electrical Resistivity Tomography

Electrical resistivity (the inverse of EC) is a physical property of the subsurface that quantifies how strongly a material opposes the flow of an electrical current. This is controlled by porosity, moisture content, temperature, pore water fluid conductivity, and soil texture (Archie 1942). ERT is an active source geophysical method that uses an array of electrodes to image subsurface bulk EC. Data collection is achieved by inserting sensors, called electrodes, into the ground and injecting a direct current (I) between two electrodes and then measuring the voltage drop (ΔV) between two other receiving electrodes. The basic unit of ERT data is transfer resistance (ohm), which is the measured voltage drop (ΔV) across the receiving electrodes divided by the injected current (I).

ERT data was collected using roll-along configurations (Dahlin 1996) of 96 electrodes at 10-m spacing. This electrode spacing allowed both deep and shallow features to be imaged. This electrode spacing also allowed for a comparison with seismic images that were assessed to have a similar depth of investigation. ERT measurements using nested arrays (Wenner, Schumberger), dipole-dipole, and multiple gradient arrays were collected to optimally resolve subsurface contrasts in bulk EC. Each dataset consisted of 5366 measurements and was filtered for low current (< 2 mA), high contact resistance (>20 kOhm), and high standard deviation (> 5%). A full set of reciprocal measurements was collected, which is where the current and potential electrodes are swapped. In theory, these measurements should be equal, and deviations greater than 20% were removed from the inverted dataset. Roll-along surveys produce duplicate measurements along the profile; any deviations greater than 20% between duplicates were removed from the inverted dataset. Table 1 provides additional details for each of the ERT profiles. These profiles were independently analyzed.

Table 1. ERT profile details. Refer to Figure 2 for locations.

ERT Profile Designation	Number of Roll-Along Surveys	Total Number of Electrodes / Length (m)	Total Number of Measurements Modeled
EW-1	2	144 / 1430	9,050
NS-1	3	224 / 2230	14,029
NS-2	3	224 / 2230	14,571

To solve for subsurface spatial distributions of bulk EC, ERT data of resistance values was analyzed using E4D (Johnson 2014), which is a finite element geophysical modeling and inversion code. Each ERT profile was independently inverted. ERT imaging resolution is governed by many factors, including electrode spacing, proximity to electrodes, background electrical noise, and measurement sequence. For the 2D ERT imaging collected here, the highest image resolution is directly beneath the line, with higher resolution closer to the surface, decreasing with depth. E4D outputs ERT sensitivity using the diagonal of the Jacobian J, which contains the derivative of each measurement with respect to the modeled bulk EC in each finite element volume. To visualize sensitivity spatially, the diagonal of $J^T J$ is normalized by each squared element volume, which shows the influence of the measurement on the inverted bulk EC. In the ERT images shown below, regions of low sensitivity are grayed-out. This represents regions that are generally not well-informed by the data and the bulk EC is less reliable. In addition, ERT profiles are clipped at a dip of 45-degrees at each end since these areas contain a much lower density of measurements and are typically not shown in ERT profile images.

3.2 Seismic

Seismic waves are sensitive to the elastic properties of the subsurface, which depend on lithology, confining pressures, moisture content, and porosity (Mavko et al. 2009). Seismic surveys produce three primary types of waves: (1) compressional waves (p-waves) are body waves that have particle motion parallel to the direction of wave propagation, and they propagate at velocity Vp; (2) shear waves are body waves that have particle motion perpendicular to the direction of propagation, and they propagate at velocity Vs; (3) surface waves include Love and Rayleigh waves and are superposed body waves that propagate along the surface at a speed slightly less than Vs (Steeples 2005). Rayleigh waves and reflected and refracted p-waves were the dominant phases measured. Rayleigh waves can be used to estimate Vs, refracted p-waves can be used to measure Vp, and reflected p-waves map subsurface boundaries where a contrast in Vp and/or density exists. Generally, both Vp and Vs increase with increasing confining pressure and decreasing porosity and Vp increases when saturated while Vs is relatively insensitive to saturation.

South of Route 4S, seismic data along Seis-NS-1, Seis-NS-2, Seis-EW-1, and Seis-EW-2 was collected using a 96-channel Geometrics GEODE system. The data was recorded using 4.5-Hz vertical component geophones spaced 5 m apart at a sample rate of 2000 Hz for 2 seconds after each shot. Shot spacing was 10 m. A United Service Alliance accelerated weight drop (AWD) was used to generate the seismic signal (see Appendix A for more details). To maintain offsets of at least 300 m, source positions were reoccupied after moving geophones ahead on the profile. Maximum offsets ranged between 320 and 700 m and provide the data necessary to image Vp to ~100- to 150-m depth. This recording geometry is also suitable for obtaining Vs from multi-channel analysis of surface waves (MASW) (Pasquet and Bodet 2017) and for mapping reflections in the subsurface.

Seismic data along Seis-Canton was collected by Bay Geophysical and acquired using a vibroseis as a source and with 96 geophone channels on either side of the source location (CH2M 2009). Geophone and shot spacing were 4 m and the data was originally processed to produce reflection images in time (Appendix B). The acquisition parameters were optimized for reflection imaging and the data does not contain sufficient low-frequency surface wave energy for MASW processing. However, the data does contain refractions suitable for travel-time tomography. Refraction travel times from this ~3-km-long profile along Canton Ave were used to obtain a Vp image and to assist in FY23 acquisition planning (Figure 3).

In addition, a check shot velocity profile for well 699-37-47A was available near the intersection of Canton Ave and Route 4S (Figure 3). Downhole geophone interval was 3.048 m (10 ft), and a 1D Vp profile was obtained from the first arrival travel times (Ch2Mhill 2010).

Table 2. Seismic profile details.

Seismic Profile Designation	Seis-NS-1	Seis-NS-2	Seis-EW-1	Seis-EW-2	Seis-Canton
Profile length (m)	2755	2275	1555	1555	3036
Number of geophone stations	552	456	312	312	760
Geophone spacing (m)	5	5	5	5	4
Number of source stations	278	214	156	178	748
Source spacing (m)	10	10	10	10	4
n-travel times modeled	9,459	9,160	5,977	8,922	16,447
Tomography root mean square error (rms)	4.1	3.0	3.7	4.4	3.5
n-dispersion curves modeled (25-m interval)	139	87	60	60	0
Nominal Common Midpoint (CMP) fold	45	45	45	45	96

The procedure to produce Vp and Vs images can be reviewed in Robinson et al. (2023). Reflection images were produced using a standard processing flow including geometry assignment, dead channel mutes, CMP sort, surface wave mute, normal moveout (NMO), and stack. In addition to the previous steps, a velocity filter (Appendix A) was used to suppress guided waves with an apparent velocity of ~800 m/s in the shot gathers. There are two primary reflections observable in all raw shot gathers (Figure 4). The shallow reflection (green) has a moveout velocity of ~950 m/s while the deeper reflection (blue) has a moveout velocity of ~1800 m/s. The standard NMO approach is not able to correctly map both events to their zero-offset travel time due to the large velocity contrast (Miller and Xia 1998). The approach used instead was to process the dataset twice, once with a moveout velocity gradient targeting shallow structure and once with a constant moveout velocity of 1800 m/s for the deeper structure (Bradford and Sawyer 2002). Depth to the reflectors was estimated using the NMO velocity to convert time to depth. The NMO velocity is a reasonable estimate for time to depth conversion; however, it is an estimate, and the converted depths are subject to uncertainty.

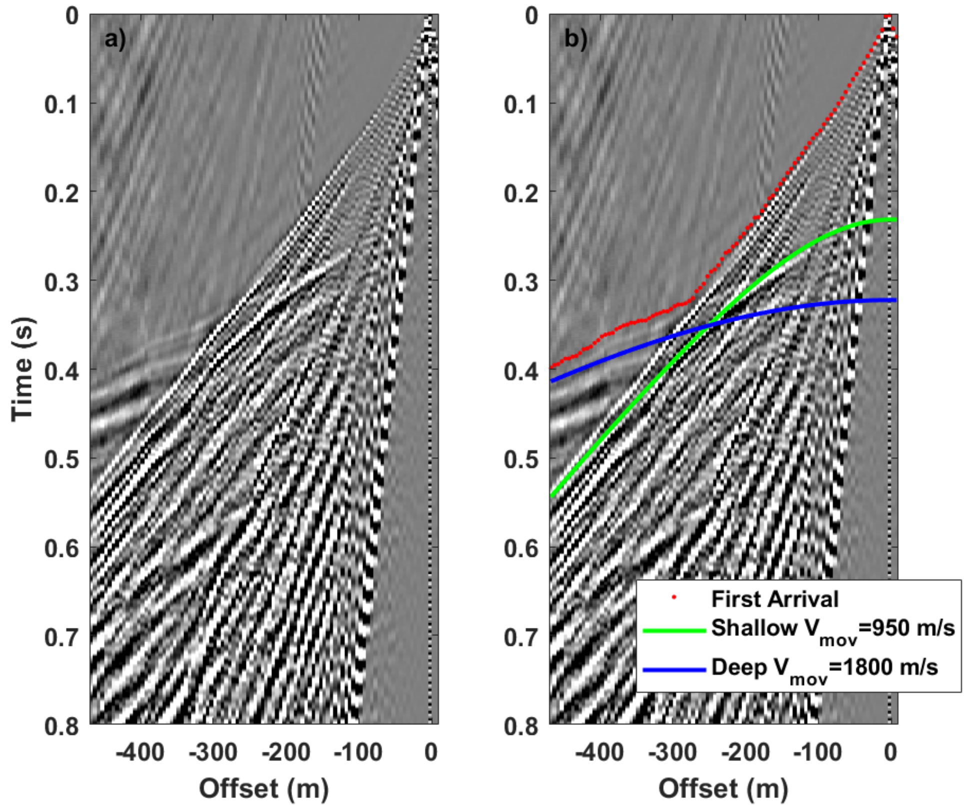

Figure 4. Shot gather from Seis-NS-2 a) without interpretation and b) with first arrival picks (closely spaced red dots), shallow reflection (green line), and deeper reflection (blue line) highlighted.

3.3 Time-Domain Electromagnetics

TEM is an active source geophysical method that can be used to image subsurface bulk EC. A towed time-domain electromagnetic (tTEM) system designed by Aarhus University (Auken et al. 2019) was used to collect the TEM data. This system is designed to provide a lateral resolution of about 10 m and a vertical depth of investigation ranging from the top 2–3 m to about 50–70 m, depending on the subsurface bulk EC, and is sensitive to electrically conductive targets. A tTEM measurement is made by passing a time-varying current through the transmitter Tx coil, which induces a primary magnetic field in the subsurface. When Tx is turned off, eddy currents are induced in subsurface electrically conductive bodies, which induces a secondary magnetic field. The Rx coil in the tTEM system measures the time decay of the secondary field as the time derivative of the z-component ($VA^{-1}m^{-2}$). The time-decay of the secondary field can be used to infer the distribution of the bulk EC. The early time recording (15 low moment time gates) corresponds to a signal from the shallower subsurface, and the later time recording (30 high moment time gates) corresponds to a signal from the deeper portions of the subsurface.

The Aarhus Workbench software was used to process the data. This software allows the user to view, filter, and invert the data. Noise from various sources (e.g., capacitive couplings from metallic infrastructures, power line noise, random noise) was removed and then stacked over a predefined window to get averaged sounding (stacked) data. Within Workbench, the stacked data was used for a 1D laterally constrained inversion, which also performs depth of investigation calculations (Auken et al. 2015). For a detailed description of the tTEM system and its data processing, see Auken et al. (2019).

tTEM data was previously collected on the Hanford Site between the 200 Areas and west of 200 East (Robinson et al. 2023). It was determined that tTEM would have utility where the overlying layer (e.g., Hf) was shallow. Where the Hf was deeper, the low moment data was not useful and the high moment data had low signal magnitudes. Given the low cost and low time commitment of tTEM data acquisition, it was opted to collect this dataset along the same gravel roadways where seismic data and ERT-NS-1 was collected (Figure 3). There were no indications during pre-field reconnaissance or field work that subsurface metallic infrastructure (e.g., pipelines) was present; however, several aboveground power lines were observed.

4.0 Results

This section presents the ERT, seismic, and TEM results. Each of these geophysical datasets was independently analyzed and interpreted for a joint interpretation as described in Section 5.0.

4.1 Electrical Resistivity Tomography

ERT images are presented as a fence diagram (Figure 5a) and profiles (Figure 5b and Figure 6). The independently processed ERT images and sensitivities match well where the profiles intersect. Figure 5a plots the ERT images in the same scale where it is observed that the subsurface is more conductive below NS-1 and NS-2 compared to the eastern side of EW-1. The region along EW-1 that intersects NS-1 and NS-2 coincides with the higher bulk EC observed along these profiles. For the range and maximum bulk ECs in these images, it is highly unlikely there is any buried metallic infrastructure along these profiles.

Viewing NS-1 and NS-2 at a different color scale allows for additional structure to be observed (Figure 6). NS-1 and NS-2 were positioned parallel to each other, in part, to see if there was continuity and/or similarity in bulk EC structure, which imparts additional confidence and insight into the ERT images. The southern areas have higher bulk EC shallow features compared to the northern areas. A shallow higher bulk EC may mask lower bulk EC structures below due to the modeling constraints applied; therefore, the bulk EC below 50 m on the southern ends may be lower than shown, and this region may, in fact, look similar to the low (blue) bulk EC region on EW-1. The northern areas have a shallow (< 50 m) lower bulk EC and higher bulk EC at depth. There is limited lateral structure in these images and vertical structure is limited to shallow depths. The bulk ECs in the ERT images fit the data well along each profile (Figure 7).

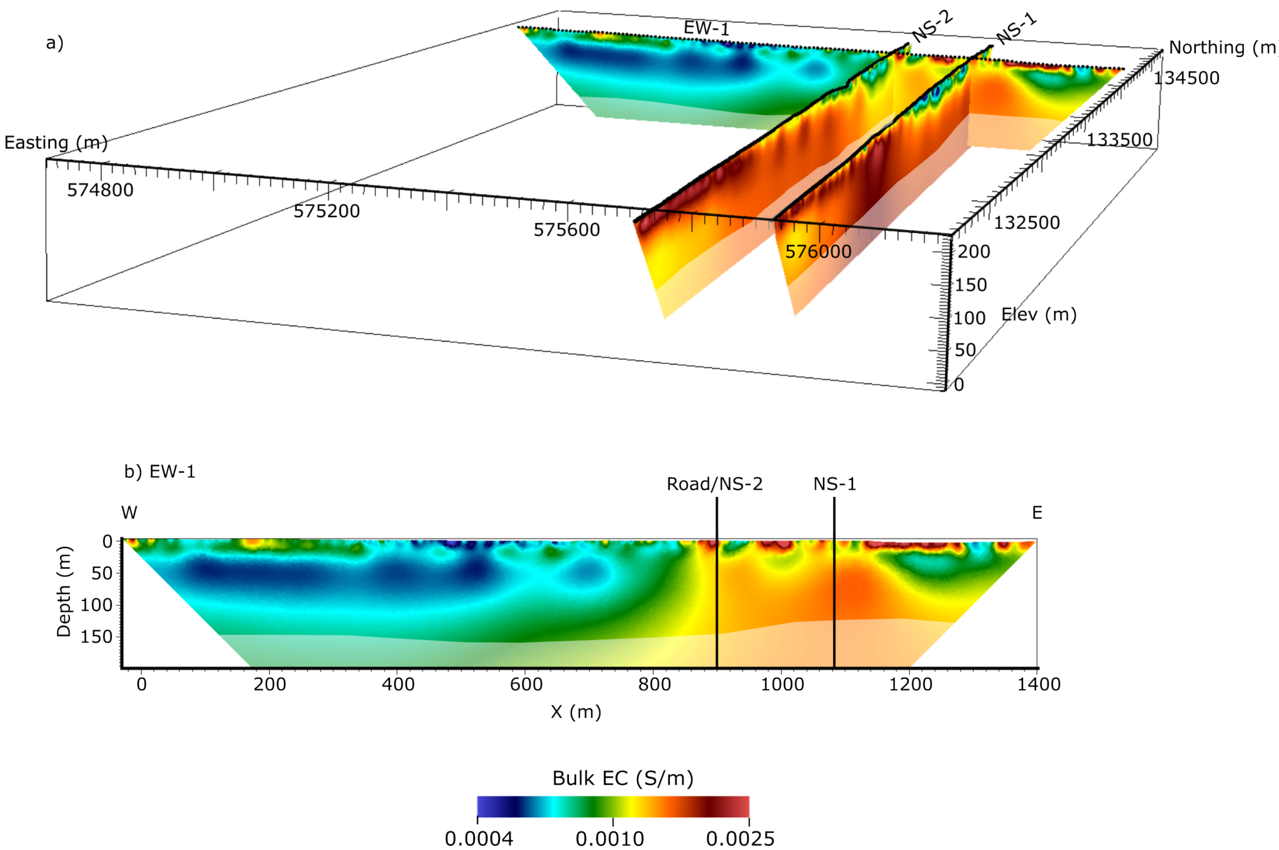

Figure 5. a) ERT fence diagram showing images for ERT-EW-1, ERT-NS-1, and ERT-NS-2; b) profile view of ERT-EW-1. Shaded white areas at depth are areas of low sensitivity to the data.

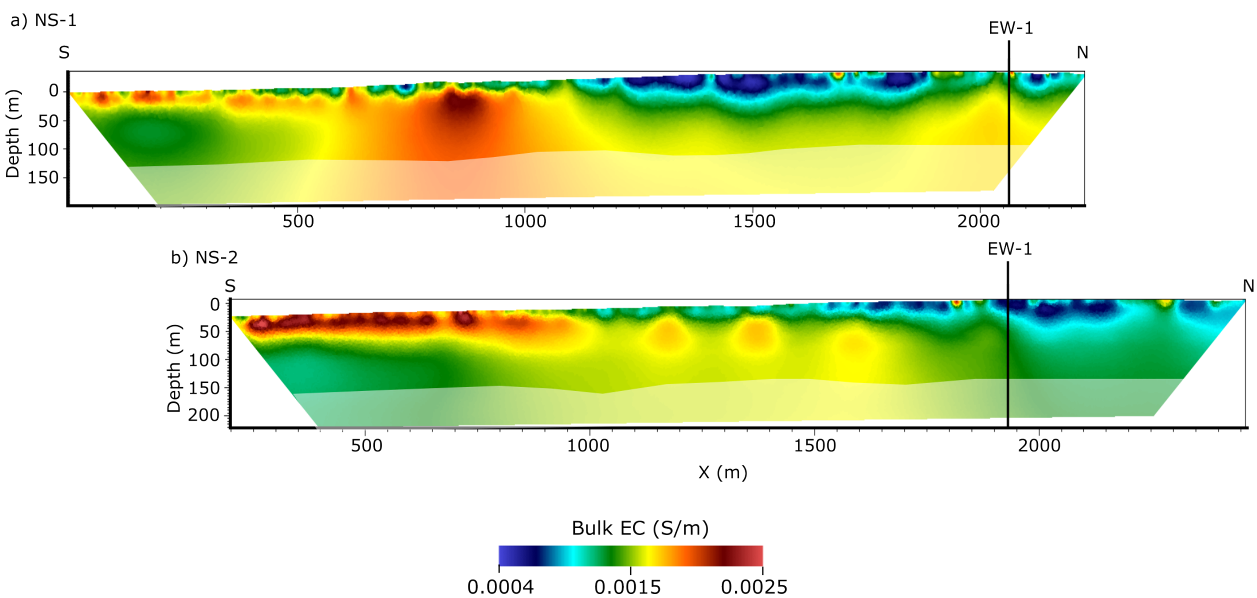

Figure 6. ERT profile images for ERT-NS-1 and ERT-NS-2. Note the change in color scale from Figure 5.

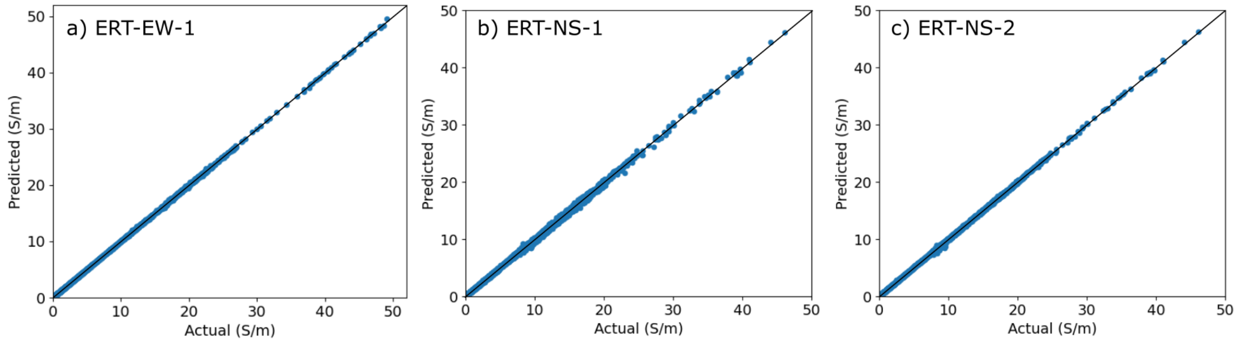

Figure 7. Data fits for ERT profile images. The black 45-degree line originating from the origin (0,0) represents a perfect data fit.

As a comparison to Figure 5 and Figure 6, Figure 8 plots these images alongside an ERT image from Robinson et al. (2022), which is from a profile southeast of the current profiles. The purpose of this previous field investigation was to use bulk EC structure as an indicator of stratigraphic structure in an area where there was uncertainty in determining where subsurface plumes were migrating from the 200 East Area. In that study, the ERT area was designated as Area 3 and consisted of a northeast (NE), southwest (SW), and parallel (P) profile, which was directionally referenced to Route 4S. The profile crossed Route 4S; however, ERT cables were not permitted to be left in place along the roadway, which necessitated that three profiles be collected. The closest Area 3 section to Figure 5 and Figure 6 is Area 3 – SW. These are shown together in Figure 8. See Robinson et al. (2022) for other ERT images south of 200 East, which generally display similar bulk EC structure.

The electrode spacing used for Area 3-SW was 25 m in 64 electrode roll-along segments (1575 m); therefore, the depth of investigation was deeper than the current profiles with 10-m spacing (which had 95 electrode roll-along segments with a length of 950 m). The bulk EC profile along Area 3 – SW shows slightly dipping bulk EC layering, with some undulations at depth. These undulations were interpreted as a potential location for a transmissive region. There are also shallower variations in the low bulk EC layer where a region of higher bulk EC is within the low bulk EC layers from approximately 1000-2000 m (Figure 8b). This increase in bulk EC would be consistent with an increase in porosity and a potential location of an HCZ signature. The Hanford South site geologic framework model is overlain for comparison. The relevancy of Area 3-SW to these profiles is that NS-1 and NS-2 appear to have a different structure than Area 3-SW. While the eastern end of EW-1 appears similar to Area 3-SW, NS-1 and NS-2 appear to have limited layering, with a shallower and higher bulk EC. Comparing NS-1 and NS-2 to other profiles in Robinson et al. (2022) reveals a similar finding. South of 200 East along NS-1 and NS-2, a potential cause of the high bulk EC structure at depth has not been identified.

Note that the ERT images are interpreted qualitatively to determine where bulk EC contrasts are occurring and/or relative difference in structure. Borehole calibration data, where bulk EC is collected within known geologic units and/or contacts and moisture contents, could lead to a quantitative interpretation of these images.

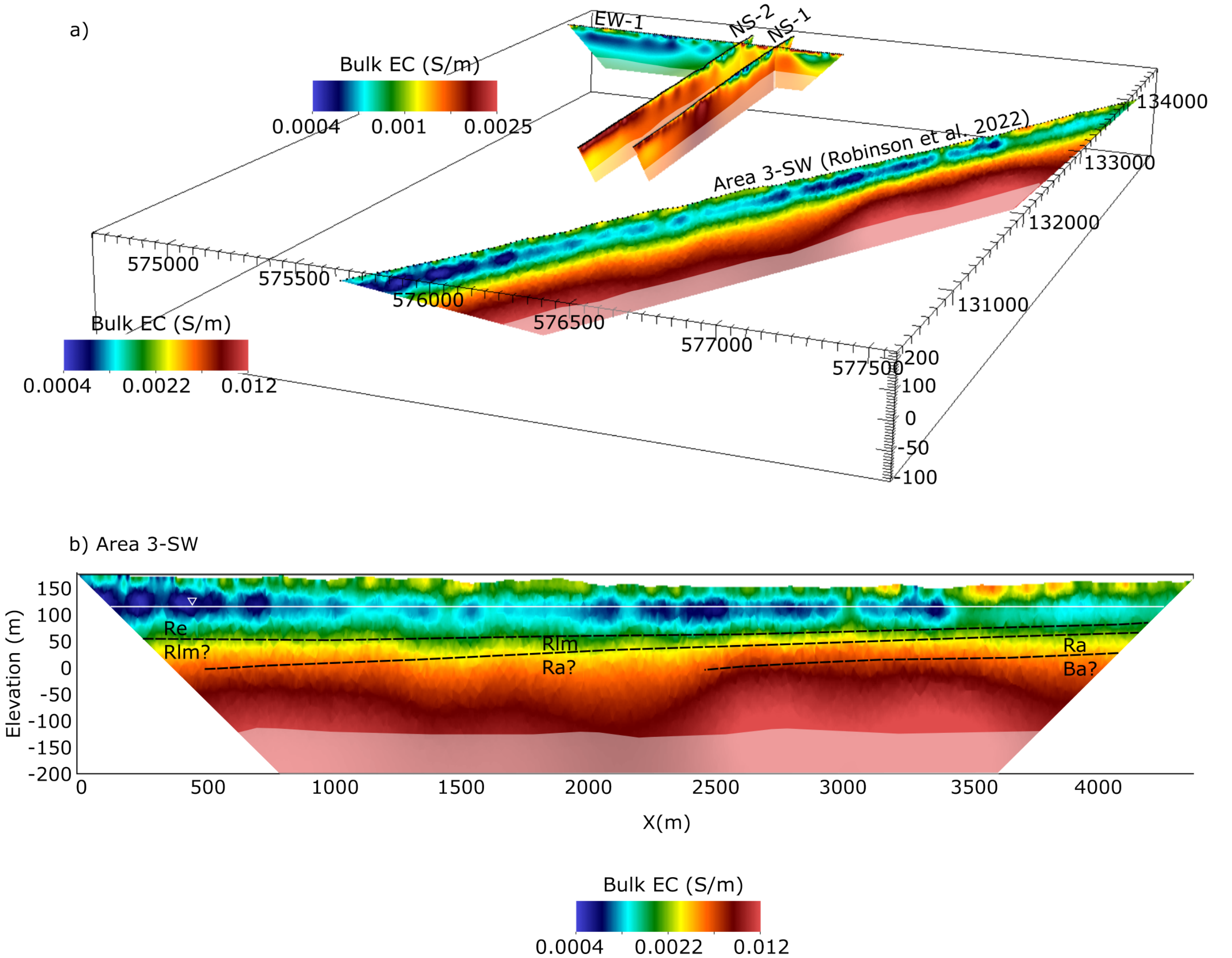

Figure 8. a) Comparison of ERT images using 10-m electrode spacing (EW-1, NS-2, and NS-1) and at 25-m electrode spacing south of the 200 East Area and b) profile image of Area 3-SW [modified from Robinson et al. (2022)]. The larger 25-m electrode spacing and longer cable can image deeper, and since the bulk EC was more conductive at depth, different profile bulk EC color scales were used to gain an overall understanding of bulk EC contrasts.

4.2 Seismic

This section presents the reprocessed seismic data collected along Canton Ave, followed by images and interpretations from more recently acquired seismic data.

4.2.1 Seis-Canton Profile

Along the Seis-Canton profile, there are several boreholes with stratigraphic interpretations for comparison to the seismic imaging results. A 1D Vp profile for borehole 699-37-47A (Ch2Mhill 2010) was also available. This data is overlain in Figure 9, and this information was used to interpret the seismic images herein. Borehole 699-37-47A was originally drilled through the top of Ba but was later backfilled, so the current depth of the well is 100 m bgs and terminates in the upper Ringold Formation. The Vp profile was extended to the top of Ba using velocity measurements within the same stratigraphic section in borehole C4562, which is approximately 1.5 km to the west.

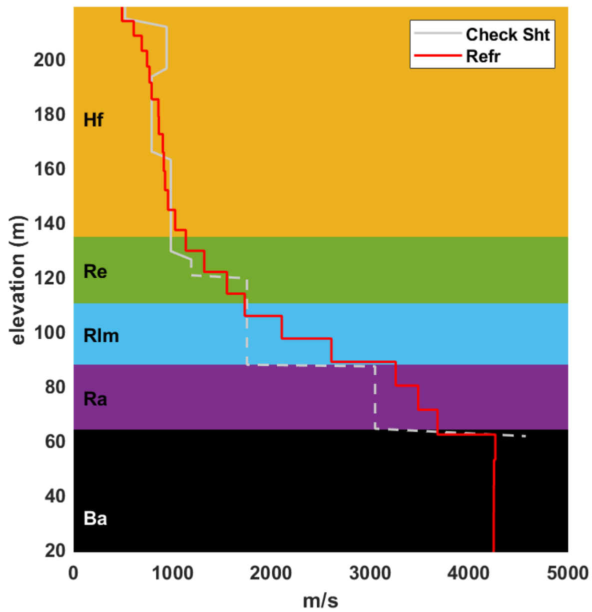

Figure 9. Borehole stratigraphic interpretations in 699-37-47A plotting with the 1D Vp profile. The dashed gray line indicates the section where Vp was extrapolated using measurements for C4562.

The reprocessed Seis-Canton profile is shown in Figure 10 and a comparison of this result to the image presented in CH2M (2009) is shown in Appendix B. On the southern end near 699-37-47A, Vp is less than 1000-1200 m/s from the surface to an elevation of ~140 m. Between elevations of 140 and 60 m, Vp increases with depth from ~1200 to 4200 m/s; below 60 m Vp remains constant. This vertical Vp structure agrees closely with Vp derived from the check shot (Figure 9). Using the check shot as a reference, Vp < ~1200 m/s is associated with Hf, the elevation that Vp begins to increase above 1200 m/s correlates with the top of Rwie, and the elevation that Vp reaches 4200 m/s correlates with the top of Ba. Though the individual units within the Ringold Formation are not distinguishable from travel-time tomography, their presence is detected.

Along the north side of Seis-Canton, at profile distances greater than 1000 m, the vertical Vp gradient becomes sharper. The stratigraphic borehole interpretations of 299-E35-93, 299-E25-2, and 299-E24-33 between 1200–1500 m along the profile suggest that the Ringold Formation is not present. The CCU is interpreted to be present in 299-E35-93 and 299-E25-2 between 1100 and 1300 m; however, a vertical Vp gradient is not observed. Along the entire profile, the transitions to Vp > 4200 m/s are coincident with the top of Ba as indicated by the current GFM.

Reflections for Seis-Canton (grayscale in Figure 10) correlate well with the Vp tomogram. Near 699-37-47A, there is a bright reflection that correlates with the top of Rlm. Near 1000 m along the profile, the character of this reflection changes to a lower-amplitude, less continuous feature. This would be expected for a reflector with a rough surface such as the top of Ba. The reflector elevation correlates well with the transition to Vp > 4200 m/s, also consistent with the interpretation that it represents the top of Ba.

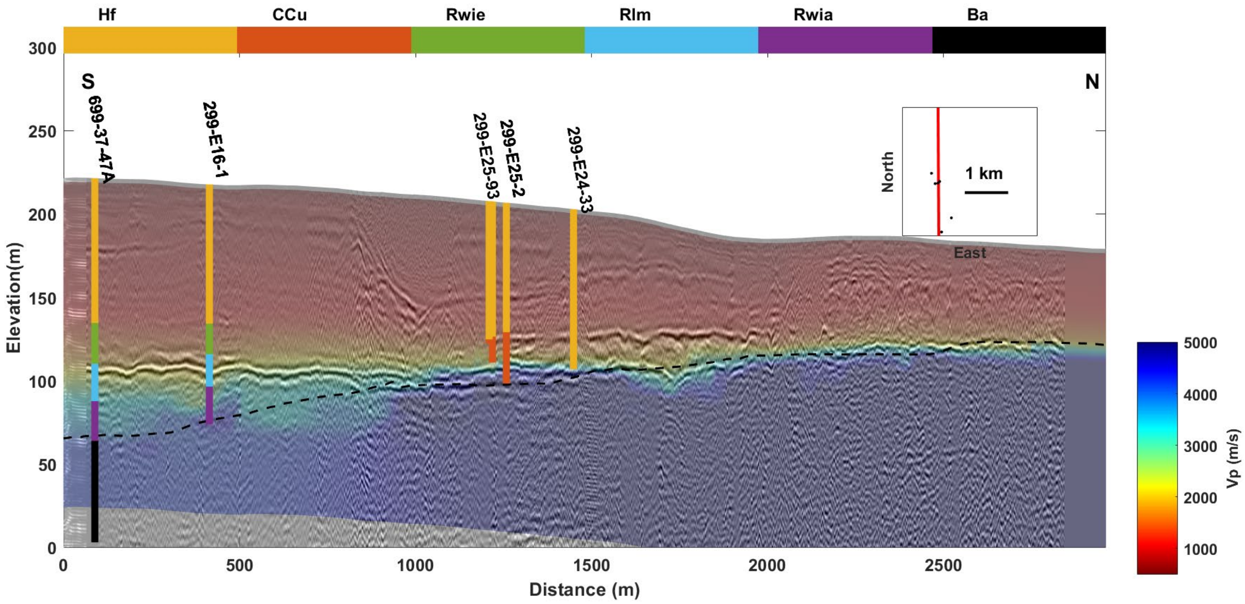

Figure 10. Seis-Canton reflection image (grayscale) with overlain Vp (color scale) and stratigraphic interpretations from nearby boreholes. Borehole locations with respect to profile are shown in upper right inset. Black dashed line indicates the top of Ba extracted from the current GFM. Vertical exaggeration 10:1.

4.2.2 Seismic Profiles South of Route 4S

4.2.2.1 Shallow Reflection Processing

Figure 11 shows Vp and reflection images processed for shallow reflectivity (refer to Section 3.2) for Seis-NS-1, Seis-NS-2, Seis-EW-1, and Seis-EW-2. These profiles show a similar seismic structure compared to the southern portion of Seis-Canton. Above an elevation of ~100 m, Vp is less than ~1200 m/s. At ~100 m elevation, Vp increases to 2000–3000 m/s, coincident with a bright reflector on the reflection image. Extrapolating from the interpretation of Seis-Canton and 699-37-47A, this likely represents the top of Rlm. The maximum Vp imaged south of Route 4S is ~3000 m/s, suggesting that Ba is too deep to be imaged for the survey geometry used.

Reflection images for Seis-NS-1 and Seis-NS-2 both show reflectors at approximately 150-m elevation on the southern end that dips to the north (Figure 11a and c). It is unclear what this boundary represents.

A fence-diagram showing all five seismic profiles (Vp and shallow reflections) summarizes the observed seismic structure in the study area (Figure 12). North of Route 4S, the top of Ba is imaged as dipping to the south (dark blue in the figure). Near Route 4S, Ba becomes too deep for imaging with the survey geometry used. Ringold sediments are detected starting around 1000 m north of Route 4S and extending to the southern extent of the survey area (yellow to light blue). A north dipping reflector is imaged above the elevation of Ringold sediments; its nature is uncertain.

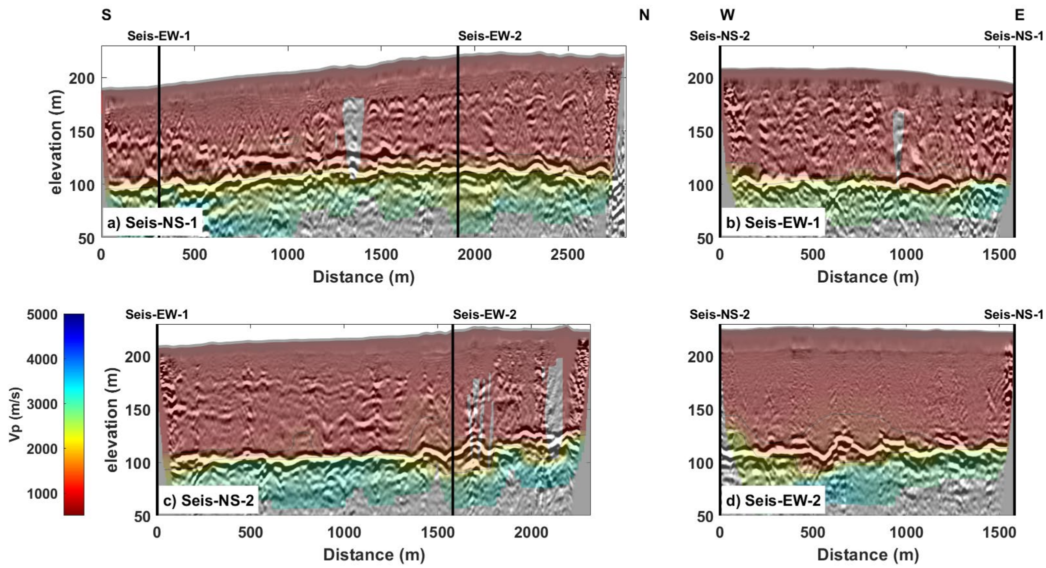

Figure 11. Vp (color scale) and shallow seismic reflection images (grayscale) for a) Seis-NS-1, b) Seis-EW-1, c) Seis-NS-2, and d) Seis-EW-2. For locations, see Figure 3. Vertical exaggeration = 12:1.

4.2.2.2 Deep Reflection Images

Figure 12 shows the deep reflections observed on the four seismic profiles. This reflection has a moveout velocity of ~1800 m/s, and the standard NMO approach to reflection processing cannot accommodate the steep velocity gradient required to image both this reflection and the shallower reflectivity shown in Figure 11 (i.e., Miller and Xia 1998). Here, the data has been processed with a constant NMO velocity of 1800 m/s. This NMO velocity produces the best image of the deep reflector, but also causes the first arriving refracted wave to stack into the image. It is important to note that the features marked “refr” represent processing artifacts while the features marked “refl” represent the reflection.

The deeper reflection dips gently to the south, much like the top of Ba imaged along Seis-Canton. However, the estimated elevation at the top of the reflection is below sea level, whereas top of Ba is observed at ~60-m elevation in 699-37-47A. This reflection may be providing information on deeper, interbedded Ba structure.

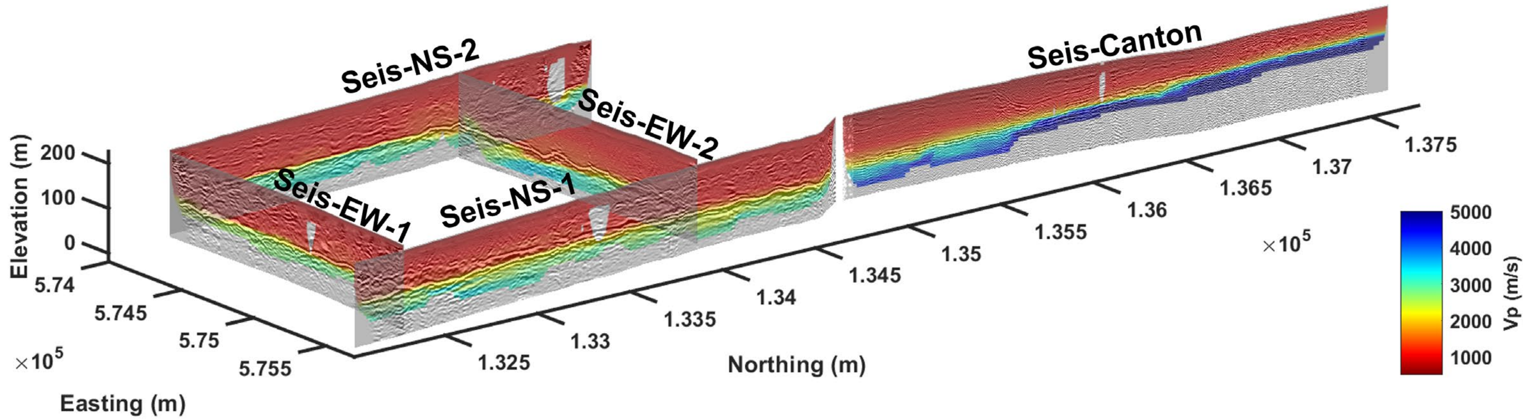

Figure 12. Vp (color scale) and shallow seismic reflection (grayscale) images shown as a fence diagram. Vertical exaggeration = 2:1.

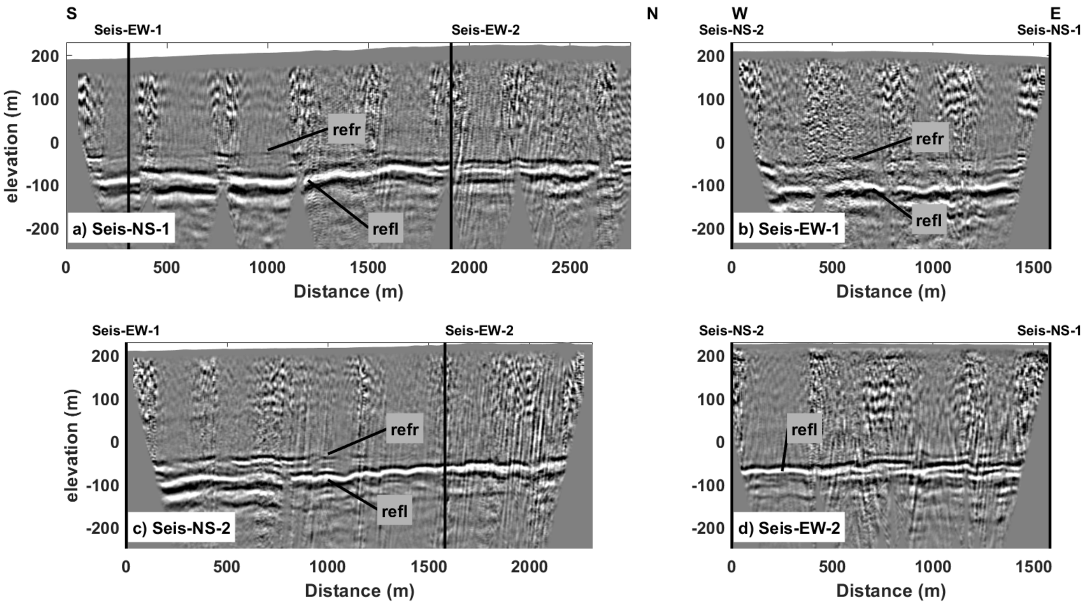

Figure 13. Deep reflection images for a) Seis-NS-1, b) Seis-EW-1, c) Seis-NS-2, and d) Seis-EW-2. For locations, see Figure 3. In some areas, the refracted arrival has stacked into the image (refr); these are processing artifacts. The reflection is labeled "refl". Vertical exaggeration = 12:1.

4.2.3 Vs Results

Figure 14 summarizes the Vs profiles extracted from Rayleigh wave dispersion along Seis-NS-1, Seis-NS-2, Seis-EW-1, and Seis-EW-2. The plot shows the average Vs along the entire length of each profile (solid lines) and +/- 1 standard deviation (dashed lines). There is very little lateral variability in Vs in this area, as indicated by the narrow spread of the standard deviation lines. Vs increases from around 180 m/s at the surface to ~450 m/s at a depth of 20 m. Figure 14 also shows the mean Vs for profiles collected between the 200 East and 200 West areas (Lines 3 and 4) and along Route 4S (Robinson et al. 2023). The Vs data collected south of Route 4S and the Route 4S profile (Robinson et al. 2023) show the same Vs structure. In contrast, Lines 3 and 4 between the 200 Areas show higher Vs and much more lateral variability (larger standard deviations), suggesting that the upper 25 m south of 200 East is composed of different material than the upper 25 m between the 200 Areas. Since Vs decreases with increasing porosity (e.g., Mavko et al. 2009), shallow sediments to the south of Route 4S may have higher porosity than shallow sediments outside of the HCZ.

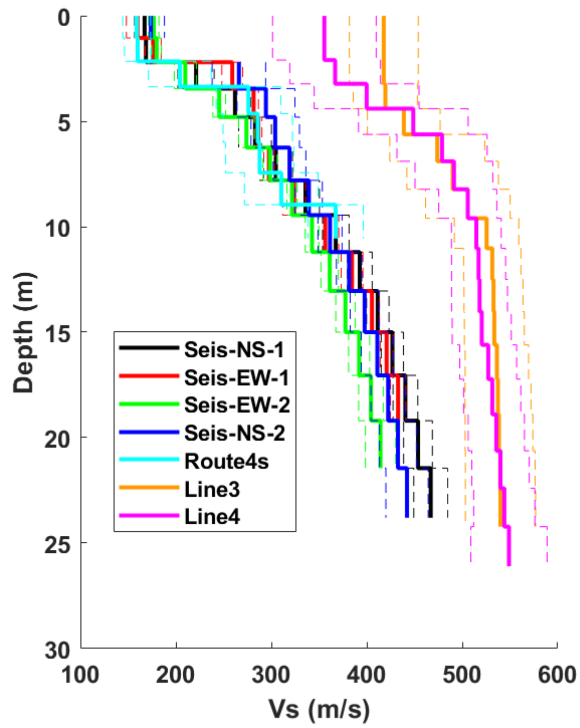

Figure 14. Mean Vs along the length of each profile for Seis-NS-1, Seis-EW-1, Seis-NS-2, and Seis-EW-2 compared to profiles Route 4s, Line 3 and Line 4 (Robinson et al. 2023). Dashed lines indicate +/- 1 standard deviation from the mean. Lines 3 and 4 show higher Vs and more lateral variability (as indicated by dashed lines) compared to all other profiles. See Figure 3 for line locations.

4.3 Time-Domain Electromagnetics

TEM data suffered from low signal magnitude and EM noise from overhead power lines. Low moment data was unusable. High moment raw data plots are shown in Figure 15 for two co-located tTEM profiles south of 200 East. Figure 15a has several spikes, which are attributable to overhead power lines. The remainder of this data has very low signal magnitude. Figure 15b also has low signal magnitude, but data quality appears higher, so an attempt was made to invert this data. The resulting model had a high bulk EC layer with decreasing bulk EC along the entire profile. The tTEM image structure and associated bulk EC values were deemed not practical when compared to (1) ERT profile values and (2) other bulk EC structure from tTEM and ERT in and around the Central Plateau. We presume the Hf is too thick in this area to gain meaningful results from the tTEM.

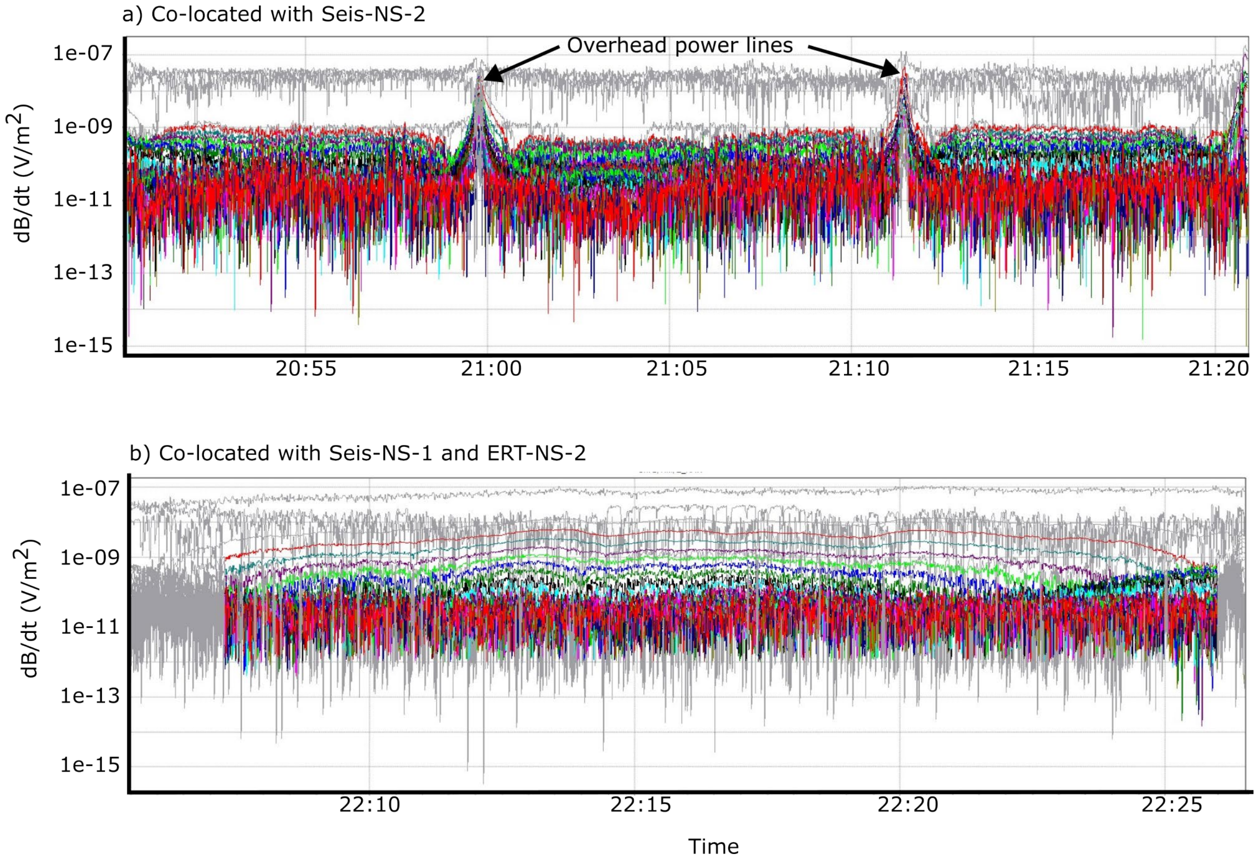

Figure 15. High moment raw data tTEM plots for profiles co-located with other geophysical datasets. Grayed out lines were auto-filtered within Workbench.

5.0 Discussion

The geophysical methods used have sensitivity to overlapping physical properties (porosity, moisture content, lithology); however, the physics and resolution of the methods are different, and therefore the information content can also be different.

The ERT images for the three profiles (ERT-NS-1, ERT-NS-2, ERT-EW-1) were compared, and where the profiles intersected, the bulk EC agreed well. The bulk EC structure was similar along parallel profiles ERT-NS-1 and ERT-NS-2. Both profiles have a shallow high (southern end) and low (northern end) bulk EC layer and below this there is limited structure. Of note was that a comparison to nearby ERT images revealed that ERT-NS-1 and ERT-NS-2 did not have a subsurface structure that was like other ERT images south of 200 East. The fact that ERT-NS-1 and ERT-NS-2 are parallel and independently processed gives confidence in the images shown; however, a review of Hanford waste sites (https://phoenix.pnnl.gov/apps/gisexplorer/index.html) did not reveal a compelling reason for this difference from other ERT images. Note that previous interpretations southeast of 200 East hypothesized dipping low bulk EC regions as potential regions of transmissive features (Robinson et al. 2022), which agreed with the conceptual model of these features; however, this is different than the higher bulk EC region observed in the ERT NS profiles. The west end of ERT-EW-1 was similar in bulk EC structure to other profiles collected south of 200 East but did not show any dip in bulk EC structure.

There is significant uncertainty in interpreting hydrostratigraphy from the ERT characterization images, in part because there is no site-specific supporting data (e.g., borehole data in the vicinity of this study) that correlates bulk EC to stratigraphic units, moisture content, and/or transmissivity. While Robinson et al. (2022) hypothesized that dipping low bulk EC regions could be potential regions of transmissive features, this was based on the location and shape of these features compared to the existing GFM, and not from a field- or lab-based correlation. This means that ERT images cannot indicate with certainty what a high or low bulk EC means within the HCZ analysis area; however, the images can identify where physical properties are different along a profile, and this is an indirect, qualitative measure of hydrostratigraphy.

Since ERT and TEM both produce images of bulk EC, these two methods are often used to complement each other and/or provide multiscale information for site investigations. Unfortunately, TEM data quality was low. These results were similar to previous investigations that found that site infrastructure (e.g., overhead power lines) and a thick overlying Hf unit resulted in unusable or low signal magnitude data. Future applications of TEM on the Hanford Site should be limited to areas where conductive units and/or the water table is shallower.

The availability of check shot data in 699-39-47A allowed for calibration with borehole stratigraphic interpretations, which could then be applied to interpreting Vp and reflection images. The seismic images show a consistent stratigraphic dip, suggesting that layers are generally horizontal. The independent analyses of reflections and refractions from the seismic dataset provide confidence in the interpretations; however, it is the ground truthing from the check shot data and borehole stratigraphic interpretations that allow for a more comprehensive and robust interpretation of stratigraphy between borehole locations and south of 200 East where there is no borehole control.

The seismic investigations may be providing a line of evidence toward deeper interbedded Ba structure that has not previously been detected using geophysical methods. To bring together the shallow and deep interpretations, a more sophisticated reflection processing approach such as pre-stack depth migration (PSDM) could be used. This would produce an image that considers the shallow and deep reflectivity observed in the data sets (Bradford and Sawyer, 2002) south of Route 4S. PSDM could also produce a Vp model independent from the Vp tomogram, which could aid interpretation.

A multiple geophysical approach was undertaken, in part, to compare the results from these methods. Figure 16 shows co-located ERT (ERT-NS-2) and seismic images (Seis-NS-1). At depth, there is limited structural similarity; at shallow (< 50 m) depths, a north-dipping reflector (best visible in Figure 11) in the seismic images coincides with the ERT bulk EC structure. Note that neither the seismic nor the ERT image show a geophysical contrast at the water table; therefore, moisture content is having less impact on the overall seismic and ERT images. While both seismic and ERT can have structural similarity [e.g. Robinson et al. (2023)], this does not necessarily have to be the case. Co-located ERT and seismic profiles provide information to the overall stratigraphic structure south of 200 East; however, additional information is needed to rectify the difference observed in geophysical parameters.

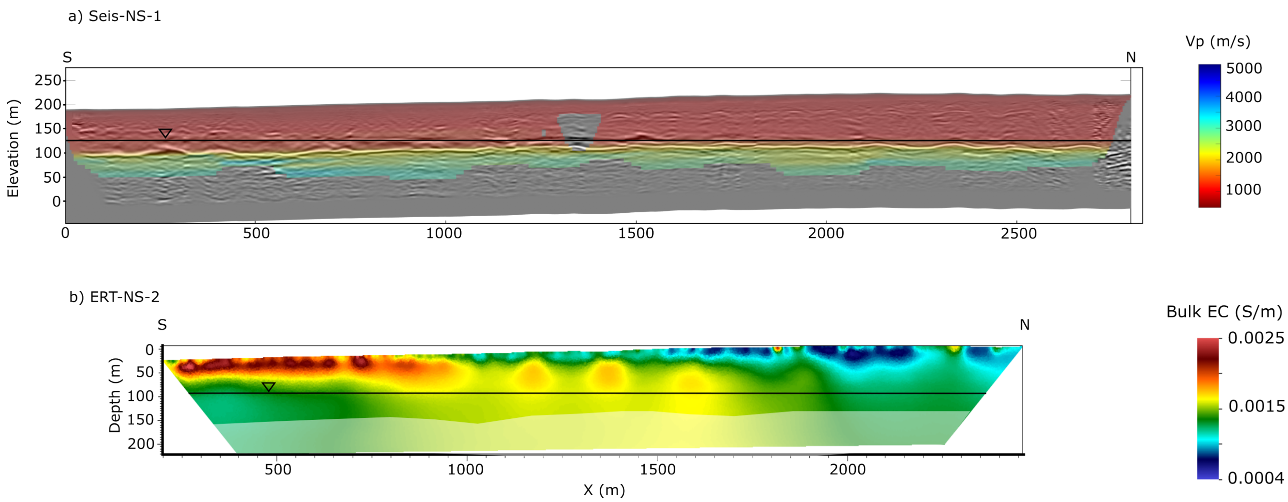

Figure 16. Co-located geophysical results showing a) seismic reflections (grayscale) with overlain Vp (color scale) from seismic refraction tomography and b) ERT image. In a), where Vp was not well resolved due to poor ray path coverage, only the reflections (grayscale) are shown; in b), the grayed out portion of the image at depth represents poor sensitivity to the ERT data.

Transmissive pathways within the HCZ analysis area are hypothesized to be coarse material incised into less permeable units (Figure 2), and therefore these geophysical investigations were undertaken to identify where contrasts in geophysical properties could be a proxy for subsurface changes in material properties. Shallower seismic interpretations reveal a horizontal dipping structure while providing insight into the depth to basalt and/or the presence of stratigraphic units. Deeper seismic interpretations may be providing evidence of deeper interbedded basalt structure. The seismic images do not coincide with the conceptual model of a transmissive feature, and there is no indication that a dipping or contrasting feature (different than the surrounding structure) is present. The NS-1 and NS-2 ERT images reveal shallow high (southern end) and low (northern end) bulk EC layering; mid-profile there is limited structure, and the bulk EC is higher at depths below 30 m but is not high enough to indicate metallic infrastructure. The bulk EC structure of NS-1 and NS-2 does not match with other ERT profiles that were collected southeast of 200 East, where dipping low bulk EC regions were interpreted as potential locations for transmissive features (Robinson et al. 2022). While this higher bulk EC region along NS profiles may provide evidence of a porosity and/or moisture contrast, this is likely small because it was not detected in the co-located seismic images. Further site information is needed to interpret this region of higher bulk EC.

6.0 Conclusions

A multiple geophysical approach was used within the HCZ analysis area to give insights into subsurface structure where there is limited borehole information. There is limited information on how or where the HCZ manifests in the stratigraphic sequence, yet there is evidence that a high transmissive zone exists south of 200 East. Existing seismic data from within 200 East was used and new seismic, ERT, and TEM field data was acquired south of Route 4S. While these methods have sensitivity to overlapping physical properties (porosity, moisture content, lithology), the resolution and physics used to acquire each of these datasets is different, and therefore the information content can also be different.

Table 3 summarizes the geophysical interpretations resulting from the investigation described in this report. Future investigations focused on ground truthing existing datasets (e.g., additional seismic check shot data, borehole ERT in areas of surface ERT data) and/or coupling with newer machine-learning techniques to combine the information from these datasets could calibrate interpretations, adding additional insights into the existing interpretations of geophysical datasets. Robust interpretations could potentially be incorporated into GFM development and used in flow and transport simulations to better understand contaminant migration on the Hanford Central Plateau for remedial planning and decisions.

Table 3. Summary of Geophysical Investigation Interpretations south of 200 East

Method	Interpretations
ERT	• The eastern end of the EW-1 profile has a similar bulk EC structure to an ERT profile further to the south and east of 200 East. • The shallow high bulk EC horizontal layer along the southern end of two NS profiles is likely impacting the ERT images, resulting in a higher bulk EC below this layer than actually exists. This area may be more alike to the eastern end of the EW profile. • Along two NS profiles, there is a higher bulk EC at depth, which is not caused by metallic infrastructure but may be due to porosity/moisture contrasts with surrounding units. This change in physical properties is likely small and therefore is not manifesting in the co-located seismic images. • Previously, low bulk EC dipping features southeast of 200 East were interpreted as potential transmissive regions; however, this differs from NS ERT images, which show a higher bulk EC region. • ERT images alone cannot provide evidence of transmissive features. Ground truthing with ERT borehole information could provide a more robust interpretation.
Seismic reflection and refraction (> 0 m elevation; 175-200 m bgs)	• Independent processing of seismic reflection and refractions produced results that agree well. These show a shallow horizontal structure dipping to the north and top of Ba dipping to the south. • Supporting borehole check shot data and stratigraphic interpretations allow for a robust interpretation of seismic images. All datasets support that the Ba contact is shallow to the north across Route 4S. The Vp gradient is sharper on the northern end of Canton Ave, and this is consistent with borehole stratigraphic information that indicates the Ringold is not present. • Vs data south of 200 East shows very little lateral variation. Compared to Vs between the 200 Areas and north of Route 4S, Vs south of 200E is reduced, indicating sediments that are less stiff and likely higher porosity; Vs between the 200 Areas indicates shallow sediments are stiffer and likely have a lower porosity. • Co-located seismic reflection and ERT profiles show a north-dipping structure. The reflection is approximately coincident with the bottom of a north-dipping, high bulk EC feature. There is limited structural similarity between these images at depths > 50 m.
Seismic reflection (< 0 m elevation; 175-200 m bgs)	• This data may be providing evidence of deeper interbedded basalt structure, which has not previously been detected on the Hanford Site using geophysical methods. • Shallow and deep interpretations could be combined using a more sophisticated reflection processing approach such as PSDM.
TEM	• Site infrastructure (e.g., power lines or subsurface metallic infrastructure) is a deterrent to collecting quality data. • Future applications of TEM on the Hanford Site should be limited to areas where conductive units and/or the water table are shallower.

7.0 Quality Assurance

This work was performed in accordance with the Pacific Northwest National Laboratory Nuclear Quality Assurance Program (NQAP). The NQAP complies with DOE Order 414.1D, *Quality Assurance*. The NQAP uses NQA-1-2012, *Quality Assurance Requirements for Nuclear Facility Application,* as its consensus standard and NQA-1-2012, Subpart 4.2.1, as the basis for its graded approach to quality.

This work emphasized acquiring new theoretical or experimental knowledge. The information associated with this report should not be used as design input or operating parameters without additional qualification and should be considered For Information Only (FIO).

8.0 References

Archie, G. E. (1942). "The Electrical Resistivity Log as an Aid in Determining Some Reservoir Characteristics." Petroleum Transactions of AIME **146**: 54-62.

Auken, E., A. V. Christiansen, C. Kirkegaard, G. Fiandaca, C. Schamper, A. A. Behroozmand, A. Binley, E. Nielsen, F. Effersø, N. B. Christensen, K. Sørensen, N. Foged and G. Vignoli (2015). "An overview of a highly versatile forward and stable inverse algorithm for airborne, ground-based and borehole electromagnetic and electric data." Exploration Geophysics **46**(3): 223-235.

Auken, E., N. Foged, J. J. Larsen, K. V. T. Lassen, P. K. Maurya, S. M. Dath and T. T. Eiskjaer (2019). "tTEM — A towed transient electromagnetic system for detailed 3D imaging of the top 70 m of the subsurface." Geophysics **84**(1): E13-E22.

Bradford, J. H. and D. S. Sawyer (2002). "Depth characterization of shallow aquifers with seismic reflection, Part II—Prestack depth migration and field examples." Geophysics **67**(1): 98-109.

Budge, T. J. (2020). Model Package Report: Plateau to River Groundwater Model Version 8.3. Richland, WA, CH2MHill.

Carollo, A., P. Capizzi and R. Martorana (2020). "Joint interpretation of seismic refraction tomography and electrical resistivity tomography by cluster analysis to detect buried cavities." Journal of Applied Geophysics **178**.

CH2M (2009). Reflection Seismic Survey Report, 200 East Area, Hanford Site. Richland, WA, CH2M HILL Plateau Remediation Company.

Ch2Mhill (2010). Measurement of Compressional-Wave Seismic Velocities in 29 Wells at the Hanford Site. Richland, WA, CH2MHill Plateau Remediation Company.

CPCCo (2021). 200 PO-1 Groundwater Operable Unit Data Quality Objectives Summary Report for Charactrerizing the Central Plateau High Conductivity Zone. SGW-65180, Revision 0 Draft. Richland, WA, Central Plateau Cleanup Company.

Dahlin, T. (1996). "2D resistivity surveying for environmental and engineering applications." First Break **14**(7).

DOE (2002). Standardized stratigraphic nomenclature for post-ringold-formation sediments within the central Pasco basin. Richland, Washington.

Johnson, T. C. (2014). E4D : A distributed memory parallel electrical geophysical modeling and inversion code User Guide - Version 1.0. Richland, WA, Pacific Northwest National Laboratory.

Martin, C. J. (2010). Overview of Hanford hydrogeology. Hanford Site Groundwater Monitoring and Performance Report: 2009.

Martin, C. J. (2010). Overview of Hanford Hydrogeology, DOE/RL-2010-11, Rev. 1. Hanford Site Groundwater Monitoring and Performance Report: 2009. Richland, WA.

Mavko, G., T. Mukerji and J. Dvorkin (2009). The Rock Physics Handbook: Tools for Seismic Analysis of Porous Media. Cambridge, Cambridge University Press.

McDonald, J. (2016). 200-BP-5 Treatability Test: Analysis of the Step Drawdown and Constant Rate Pumping Tests at Well 299-E33-268. Richland, WA, CH2MHill.

Miller, R. D. and J. Xia (1998). "Large near-surface velocity gradients on shallow seismic reflection data." Geophysics **63**(4): 1348-1356.

Pasquet, S. and L. Bodet (2017). "SWIP: An integrated workflow for surface-wave dispersion inversion and profiling." Geophysics **82**(6): WB47-WB61.

Robinson, J., J. St. Clair, J. Thomle, P. Jaysaval, J. Cambeiro, K. Peta, F. Day-Lewis and R. D. Mackley (2023). "Using Multiple Geophysical Methods to Refine a Stratigraphic Conceptual Site Model at a Nuclear Waste Site." Environmental Processes **10**(1).

Robinson, J., J. Thomle, D. McFarland, K. Deters, M. Rockhold, F. Day-Lewis and V. Freedman (2022). "Integration of Large-Scale Electrical Imaging into Geological Framework Development and Refinement." Environmental Processes **9**(2).

Robinson, J. L., R. D. Mackley, M. L. Rockhold, T. C. Johnson, J. N. Thomle, C. D. Johnson and P. Jaysaval (2020). Geophysical Methods for Stratigraphic Identification. Richland, WA, Pacific Northwest National Laboratory.

Steeples, D. W. (2005). Shallow Seismic Methods. Y. Rubin and S. S. Hubbard. Dordrecht, Springer Netherlands**:** 215-251.

Thayer, D., A. D. Parsekian, K. Hyde, H. Speckman, D. Beverly, B. Ewers, M. Covalt, N. Fantello, T. Kelleners, N. Ohara, T. Rogers and W. S. Holbrook (2018). "Geophysical Measurements to Determine the Hydrologic Partitioning of Snowmelt on a Snow-Dominated Subalpine Hillslope." Water Resources Research **54**(6): 3788-3808.

Wyllie, M. R. J., A. R. Gregory and L. W. Gardner (1956). "Elastic wave velocities in heterogeneous and porous media." Geophysics **21**(1): 41-70.

Appendix A – Accelerated Weight Drop

A United Service Alliance accelerated weight drop (AWD) was used to generate the seismic signal. The AWD uses a nitrogen spring to accelerate a 91-kg (200-lb) mass onto a toothed steel plate (Figure A 1). The plate is toothed for use in “shear mode,” where the mass is accelerated into the plate at a 45-degree angle. For the data in this report, only the vertical source orientation was used. The AWD was mounted on the hitch of a 1-ton pickup truck; a diesel generator, used to run the AWD’s hydraulic system, was mounted in the bed of the pickup. Before firing a shot, the hydraulic system pushes the steel plate onto the ground surface, partially supporting the weight of the pickup. Then, the hydraulic system raises the 91-kg mass upward, compressing the nitrogen spring. The mass has a steel tab bolted onto its side, which serves as catch for the hydraulically powered lifting mechanism. As the mass is raised, the lifting mechanism is guided away from the mass and the steel tab until the mass is released and it accelerates into the steel plate. At the moment of impact, a contact closure switch embedded in the plate triggers the GEODE recording system through Seismic Source’s integrated Radio Trigger Module (RTM) and Weight Drop Controller (WDC). When the contact closure switch closes, the WDC sends a radio signal the RTM, which signals the acquisition software to begin recording data.

In addition to triggering the recording system, the WDC controls the timing behavior of the AWD. The length of the shot cycle (time between raising and dropping the mass) as well as the number of automatically repeated shots can be programmed. For this survey, the WDC was programmed to automatically perform five shots per location. Multiple shots at the same location stacked together increases the signal-to-noise ratio. Each shot record was saved individually and stacked in post-processing.

Figure A.1. The United Service Alliance accelerated weight drop. The generator in the back of the pickup powers a hydraulic system that raises and lowers the toothed steel plate and raises the 91-kg mass (inside of vertical cylinder), compressing a nitrogen spring. When the mass is raised high enough, it slips off the lifting mechanism and is accelerated into the steel plate, closes a contact switch, and triggers the recording system.

It was discovered during field data acquisition that the AWD generates an unwanted precursor signal at the beginning of each lift cycle ~0.5 seconds before the weight drops. When the lifting mechanism hits the catch on the mass, it transfers the energy into the ground, generating a signal. The surface waves from the precursor signal overprint the refracted arrivals, hampering first arrival picking. One way to suppress the precursor is to use a velocity filter. The velocity filter applied as follows:

1. Shift all traces by $-h/c$ (T) where h is the source receiver offset (L) and c is the velocity (L/T) of the event to suppress.
2. Subtract a running mean from each trace.
3. Undo the time shift.

The filter was applied to common shot gathers and the goal was to flatten coherent arrivals in the shot gather that have a particular slope. Figure A.2 illustrates the process. Panel a shows the original shot gather, panel b shows the shot gather after shifting traces with c = 400 m/s, panel c shows the result of subtracting a running mean across five neighboring traces from the panel b. Finally, panel d shows the filtered shot gather after removing the time shift. Notice that in panel d, most of the coherent precursor energy that is evident in panel a has been removed.

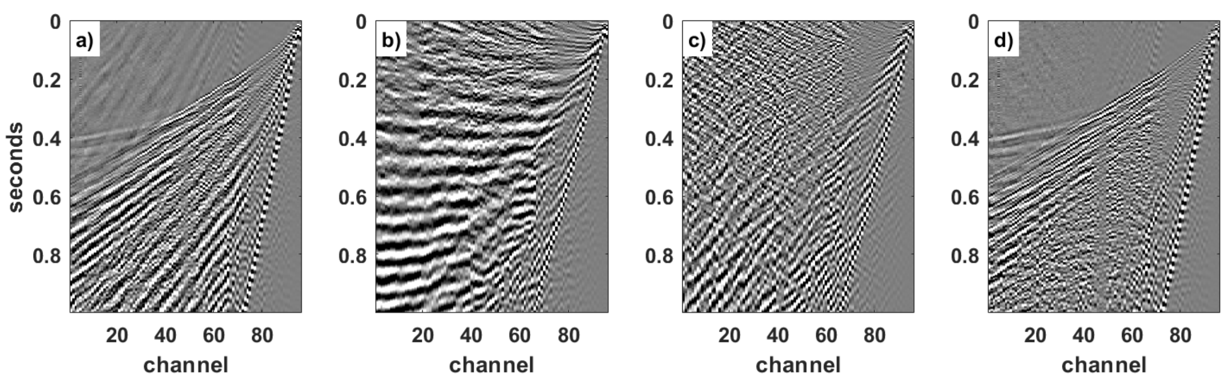

Figure A.2. The original shot-gather is shown in a), and b) shows the shot gather after the trace is shifted, c) subtracts the running mean from b), and d) is the filtered shot gather after removing the time shift.

Appendix B – Canton Seismic Reflection Comparison

In this appendix, Figure 10 and the original Seis-Canton reflection images (CH2M 2009) are compared (Figure B.1). These are displayed in grayscale in Figure B.1 with a vertical axis equal to the two-way travel time (tt2w). Our data processing steps to produce the re-processed reflection images (Figure B.1a) are outlined in Section 3.2 . Previously reported processing steps for Figure B.1b can be found in CH2M (2009).

Figure B.1a shows a single reflector at a tt2w of ~0.25 seconds on the south end shallowing to the north. In addition, there is a shallower reflector evident between profile distance ~1200 and 2000 m. Figure B.1b shows a zone of reflectivity starting at a tt2w of ~0.31 seconds to the south, also shallowing to the north. There is no shallower reflector between 1200 and 2000 m.

Figure B.2 demonstrates Figure B.1a is consistent with the raw data. Figure B.2a shows a subsection of Figure B.1a alongside a composite image of the reflection stack and a shot gather (Figure B.2b). The shot gather shows two bright reflections with a hyperbolic shape. The apexes of these hyperbolic reflections line up with the reflections visible in the stacked image. This shows the stacked image presented in Figure B.2b (and Figure 10) is consistent with the raw data.

Note that the reflectivity between ~800 and 1200 m profile distance at tt2w less than 0.2 seconds visible in both images is an artifact of out-of-plane shots.

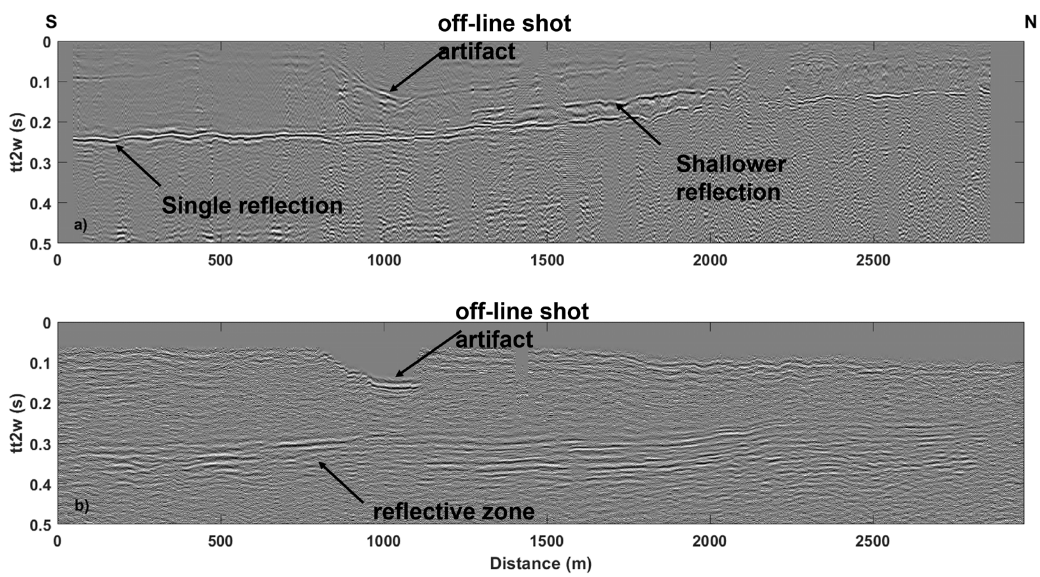

Figure B.1. a) a comparison between the Seis-Canton reflection image reprocessed in this report and b) the image presented in (CH2M 2009). The images are displayed with two-way travel time (tt2w) on the vertical axis. Both images show reflectivity shallowing to the north. Reflectivity between ~800 and 1200 m profile distance at a tt2w less than 0.2 seconds that is visible in both images is an artifact.

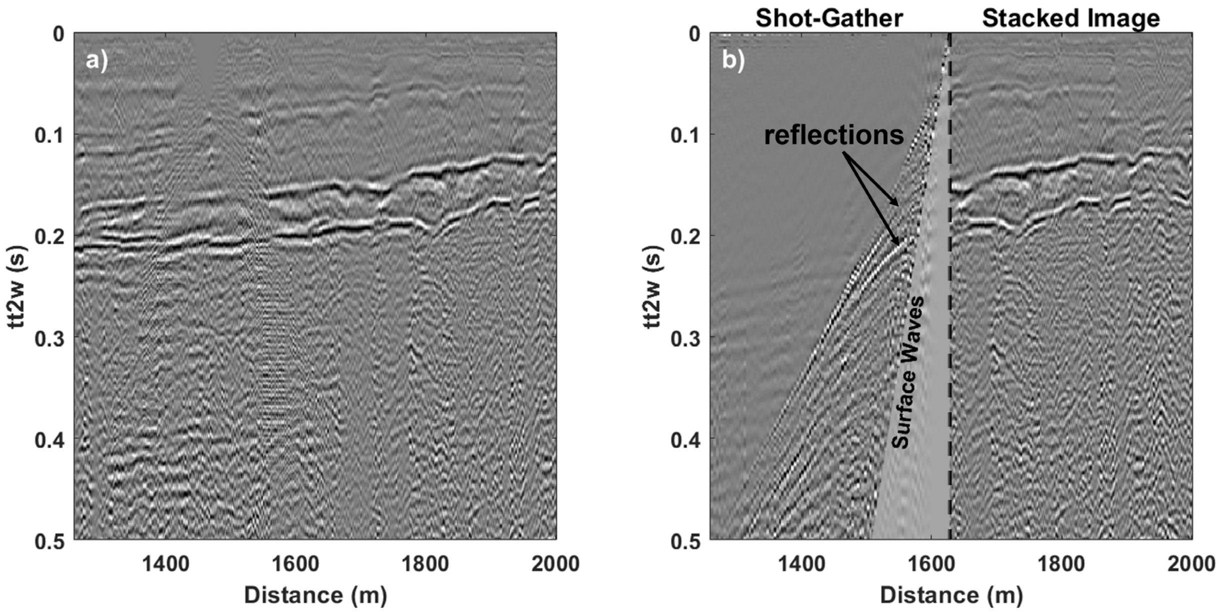

Figure B.2. a) Subset of the reflection image shown in Figure B.1a from 1200 to 2000 m; b) same as a) but with a shot gather with a source position of 1628 m spliced into the image. There are two prominent reflections in the shot gather and the apex of their hyperbolic shape aligns with the two-way travel times for the reflections that appear in the stacked image. Thus, the reflection image is consistent with the raw data. Surface waves in the shot gather are partially grayed out to not obscure viewing of the reflections.

Pacific Northwest National Laboratory

902 Battelle Boulevard
P.O. Box 999
Richland, WA 99354
1-888-375-PNNL (7665)

www.pnnl.gov